REPRINTED FROM:

HANDBOOK ON SYNCHROTRON RADIATION

VOLUME 3

Edited by

G.S. BROWN
Stanford Synchrotron Radiation Laboratory
Stanford University, Stanford, CA 94309–0210, U.S.A.

D.E. MONCTON
Argonne National Laboratory
Argonne, IL 60439, U.S.A.

1991

NORTH-HOLLAND
AMSTERDAM · OXFORD · NEW YORK · TOKYO

CHAPTER 7

SURFACE CRYSTALLOGRAPHY

I.K. ROBINSON

AT & T Bell Laboratories, Murray Hill, New Jersey, USA

Contents

1. Introduction 223
2. Diffraction from monolayers 224
   - 2.1. Basic formulae 224
   - 2.2. Integrated intensity 225
   - 2.3. Counting rate 227
   - 2.4. Background 228
   - 2.5. Crystal truncation rods 228
   - 2.6. Reconstructed surfaces 230
   - 2.7. Surface roughness 231
3. Experimental techniques 231
   - 3.1. Four-circle diffractometer 231
   - 3.2. Use of synchrotron radiation 232
   - 3.3. Resolution function 233
   - 3.4. Glancing-incidence geometry 234
   - 3.5. Total external reflection 235
   - 3.6. Background in glancing incidence 237
   - 3.7. Methods of measurement 239
     - 3.7.1. Symmetric four-circle mode 239
     - 3.7.2. Other four-circle modes 240
     - 3.7.3. Flat two-circle mode 241
     - 3.7.4. Inclined two-circle mode 241
     - 3.7.5. z-axis diffractometer 242
     - 3.7.6. Five-circle diffractometer 242
4. Surfaces 242
   - 4.1. Ultra-high vacuum characterization 243
   - 4.2. Experimental configuration 243
     - 4.2.1. Portable UHV cell 243
     - 4.2.2. Movable complete system 244
     - 4.2.3. Feedthrough based system 246
   - 4.3. Other surfaces 247

Contents continued overleaf

Handbook on Synchrotron Radiation, Vol. 3, edited by G. Brown and D.E. Moncton

© Elsevier Science Publishers B.V., 1991

Contents continued

5. Data collection 247
5.1. Experimental integrated intensity. 247
5.2. Corrections 248
5.2.1. Angular velocity 248
5.2.2. Lorentz factor 248
5.2.3. Polarization factor 248
5.2.4. Area correction 249
5.2.5. Out-of-plane measurements 249
5.3. Statistical analysis 249
5.4. Quality estimates 250
6. Data analysis 250
6.1. The phase problem 252
6.2. Patterson function 252
6.3. Agreement criteria 254
6.4. Difference map methods 254
6.5. Experimental phase determination 256
6.5.1 Using the integer-order reflections 256
6.5.2. Heavy-atom method. 256
6.5.3. Anomalous scattering 257
6.6. Direct methods 257
6.7. Refinement 258
6.7.1. Thermal motion 259
6.7.2. Partial occupancy 259
6.7.3. Error bars 259
6.7.4. Real-space refinement 259
6.8. Special crystal truncation rod techniques 260
6.8.1. Rod profile analysis 260
6.8.2. In-plane analysis with CTRs 262
7. Conclusions 263
References 263

1. Introduction

Synchrotron radiation may not be an absolute requirement for diffraction experiments on individual monolayers of atoms, but it has certainly stimulated the surge of recent interest because it transforms such experiments from the verge of feasibility to the routinely possible. Scientists may now contemplate the physics and chemistry of two-dimensional systems, knowing that the powerful techniques of X-ray diffraction can be applied to their investigation. A straight-forward application is the study of the structures of crystal surfaces, yielding information badly needed by surface scientists. Because of its close similarity to X-ray crystallography of bulk materials, this technique is becoming known as "surface crystallography".

X-ray diffraction from monolayers objects in the form of stacking faults (Guinier 1963, Jagodzinski 1949) and grain boundaries (Sass 1980) have been investigated for a number of years. Diffraction from two-dimensional layers intercalated into graphite (Erbil et al. 1983) or adsorbed onto the surface of particles in powders (Horn et al. 1978, McTague et al. 1982) have been studied extensively to learn about physics in two dimensions. Stacked layers of smectic liquid crystals (Moncton and Pindak 1979) have many two-dimensional properties measurable with X-rays. In all of these cases (Guinier 1963, Jagodzinski 1949, Sass 1980, Erbil et al. 1983, Horn et al. 1978, McTague et al. 1982, Moncton and Pindak 1979), the X-ray signal has been enhanced deliberately by assembling a relatively large number of monolayers into the scattering volume to improve the signal, which can then be measured comfortably with a rotating-anode X-ray source. More recently, it has been demonstrated that liquid-crystal films as thin as 2 layers (Moncton et al. 1982) and individual grain-boundary structures (Budai et al. 1983) could be measured with such "conventional" sources, albeit with some difficulty often requiring exposure times of 400 h (Budai et al. 1983). These latter examples have directly shown gains of two orders of magnitude or more in signal when the experiments were performed with synchrotron radiation. It was these successes that led in 1980 to the bold experiment on a free crystal surface in vacuum by Eisenberger and Marra (1981) that gave birth to the field of surface X-ray crystallography.

This chapter reviews the theory of kinematical diffraction from monolayers, describes in detail experimental methods and choice of instrumental parameters, and then lists the sequence of steps necessary to obtain structures from the measurements. The chapter was originally prepared in January 1986 and revised extensively in January 1989. Between those dates many of the original ideas had been tested, so new references have been added. Most of the examples discussed at length are from the earlier version, however. A fairly complete bibliography has been added at the end.

2. Diffraction from monolayers

2.1. Basic formulae

The wave amplitude diffracted by a single monolayer of atoms can be calculated in the Born approximation by summing the individual contributions of all the electrons in the assembly. Ignoring the factor of $\cos(2\theta)$ for the component of the wave polarized parallel to the scattering direction, the field seen a large distance R from a scattering electron at $\boldsymbol{r}$ is given by the Thomson formula (Jackson 1975),

$$A_e\, e^{-i\boldsymbol{k}_1\cdot\boldsymbol{r}} = A_0\, e^{-i\boldsymbol{k}\cdot\boldsymbol{r}} \frac{e^2}{mc^2 R},$$

$$A_e = A_0 \frac{e^2}{mc^2 R} e^{i\boldsymbol{q}\cdot\boldsymbol{r}}, \tag{1}$$

where $A_0\, e^{i\boldsymbol{k}\cdot\boldsymbol{r}}$ is the incident plane-wave amplitude. A_0^2 is the incident intensity in photons per unit area per second. The wave vectors in fig. 1 define the momentum transfer $\boldsymbol{q} = \boldsymbol{k}_1 - \boldsymbol{k}$. e and m are the electronic charge and mass, c is the speed of light. A single atom at $\boldsymbol{r}$ diffracts an amplitude obtained by integrating over its electronic distribution function, $\rho(\boldsymbol{r}')$ about $\boldsymbol{r}$,

$$A_a = A_0 \frac{e^2}{mc^2 R} \int e^{i\boldsymbol{q}\cdot(\boldsymbol{r}+\boldsymbol{r}')} \rho(\boldsymbol{r}')\, d^3\boldsymbol{r}' = A_0 \frac{e^2}{mc^2 R} f(q)\, e^{i\boldsymbol{q}\cdot\boldsymbol{r}}, \tag{2}$$

which defines the atomic form factor $f(q)$ as the Fourier transform of $\rho(\boldsymbol{r}')$. A unit cell of crystal with N_c atoms then diffracts an amplitude

$$A_c = A_0 \frac{e^2}{mc^2 R} \sum_{j=1}^{N_c} f_j(q)\, e^{i\boldsymbol{q}\cdot\boldsymbol{r}_j} = A_0 \frac{e^2}{mc^2 R} F(\boldsymbol{q}), \tag{3}$$

which defines the *structure factor*, $F(\boldsymbol{q})$, of the unit cell. A more general description of $F(\boldsymbol{q})$ would include Debye–Waller factors for the thermal motion of each of the N_c atoms (Warren 1969) (see sect. 6.8). When $N_1 N_2$ unit cells of two dimensional crystal are assembled as shown in fig. 2, the intensity of the total scattered signal is

$$I_s = A_0^2 \frac{e^4}{m^2 c^4 R^2} |F(\boldsymbol{q})|^2 \left| \sum_{j_1=1}^{N_1} \sum_{j_2=1}^{N_2} e^{i\boldsymbol{q}\cdot(j_1 a_1 \hat{\boldsymbol{r}}_1 + j_2 a_2 \hat{\boldsymbol{r}}_2)} \right|^2$$

$$= A_0^2 \frac{e^4}{m^2 c^4 R^2} |F(\boldsymbol{q})|^2 \frac{\sin^2(\frac{1}{2} N_1 q_1 a_1)}{\sin^2(\frac{1}{2} q_1 a_1)} \frac{\sin^2(\frac{1}{2} N_2 q_2 a_2)}{\sin^2(\frac{1}{2} q_2 a_2)}, \tag{4}$$

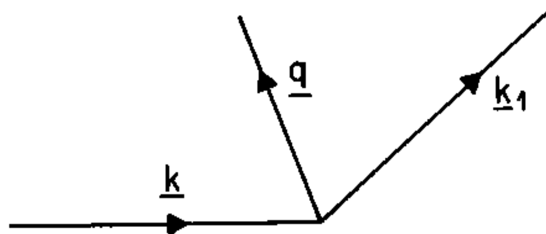

Fig. 1. Wave-vector diagram defining incident and exit wave vectors $\boldsymbol{k}$ and $\boldsymbol{k}_1$. These both describe plane waves of magnitude $2\pi/\lambda$, with λ being the X-ray wavelength. The momentum transfer $\boldsymbol{q}$ is $\boldsymbol{k}_1 - \boldsymbol{k}$.

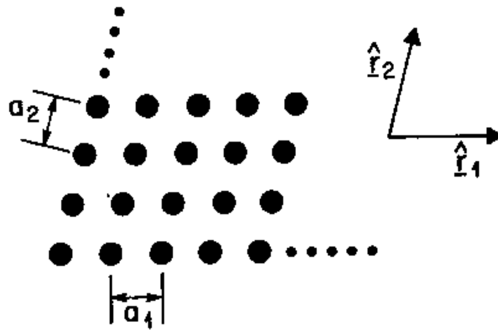

Fig. 2. Finite two-dimensional array of atoms at positions $\boldsymbol{r} = j_1 a_1 \hat{\boldsymbol{r}}_1 + j_2 a_2 \hat{\boldsymbol{r}}_2$, $j_1 = 1 \ldots N_1$, $j_2 = 1 \ldots N_2$ where $\hat{\boldsymbol{r}}_1$ and $\hat{\boldsymbol{r}}_2$ are unit vectors along the rows of atoms, and $\hat{\boldsymbol{r}}_3$ is mutually orthogonal.

where the components of $\boldsymbol{q}$ are those along unit vectors $\hat{\boldsymbol{q}}_1$ and $\hat{\boldsymbol{q}}_2$ given by the reciprocal vector construction (Warren 1969),

$$\hat{\boldsymbol{q}}_1 = \frac{\hat{\boldsymbol{r}}_2 \times \hat{\boldsymbol{r}}_3}{\hat{\boldsymbol{r}}_1 \cdot \hat{\boldsymbol{r}}_2 \times \hat{\boldsymbol{r}}_3},$$

$$\hat{\boldsymbol{q}}_2 = \frac{\hat{\boldsymbol{r}}_3 \times \hat{\boldsymbol{r}}_1}{\hat{\boldsymbol{r}}_1 \cdot \hat{\boldsymbol{r}}_2 \times \hat{\boldsymbol{r}}_3},$$

$$\hat{\boldsymbol{q}}_3 = \frac{\hat{\boldsymbol{r}}_1 \times \hat{\boldsymbol{r}}_2}{\hat{\boldsymbol{r}}_1 \cdot \hat{\boldsymbol{r}}_2 \times \hat{\boldsymbol{r}}_3}. \tag{5}$$

For large N_1 and N_2, this intensity function is strongly peaked as a function of $\boldsymbol{q}$, in exact correspondence with its three-dimensional counterpart (Warren 1969). The values of $\boldsymbol{q}$ for which eq. (4) is a maximum are given by two simultaneous *Laue conditions*,

$$q_1 a_1 = 2\pi h, \quad \text{and} \quad q_2 a_2 = 2\pi k, \tag{6}$$

with h and k integral. These define a two-dimensional reciprocal lattice, again in an analogous fashion to the three Laue conditions of three-dimensional crystal diffraction (Warren 1969). Note that there is no Laue condition on q_3: the diffraction intensity is independent of q_3 and so is *diffuse* in the $\hat{q}_3$ direction. Diffraction which is diffuse in one of the three reciprocal-space directions is the chief characteristic of two-dimensional crystals and is an important experimental identification. Henceforth, we will call such features *diffraction rods* to highlight this property. When the Laue conditions are satisfied, the two-dimensional diffraction intensity is

$$I_s = A_0^2 \frac{e^4}{m^2 c^4 R^2} |F|^2 N_1^2 N_2^2. \tag{7}$$

2.2. *Integrated intensity*

It is now necessary to include some instrumental parameters in order to calculate the intensity expected in an actual experiment. We follow the calculation of Warren (1969) to obtain the two-dimensional equivalent of an *integrated intensity*. The integrated intensity is the most useful quantity to measure in a crystallographic experiment, because it automatically accounts for crystal imperfection (in the form of mosaic

spread) and resolution function that may not be uniform. The conventional, three-dimensional form of the integrated intensity is also independent of all instrumental parameters and is, therefore, an absolute measurement (Warren 1969). We assume that a scan is made of the sample-orientation angle about an axis perpendicular to the scattering plane (see sect. 3.1) with an angular velocity Ω. This scan must commence before the peak starts to reflect and end after it has finished so that the total number of counts received is fully integrated over time. Figure 3 shows the geometry of the receiving slit in front of the detector. In the normal three-dimensional case this must be simply large enough to collect all of the diffracted beam; here, however, the diffraction is diffuse in one direction and must necessarily be cut off by the slit. The integrated intensity is defined experimentally

$$E = \int_{\text{peak}} \mathrm{d}t \iint_{\text{slit}} \mathrm{d}x\, \mathrm{d}y\, I_s = \int \frac{\mathrm{d}\alpha}{\Omega} \iint R^2\, \mathrm{d}\beta\, \mathrm{d}\gamma\, I_s, \tag{8}$$

where α is the sample rotation angle, β and γ are the angles of the exit beam $\boldsymbol{k}_1$, as shown in fig. 3, and R is the viewing distance. The reciprocal space volume element $\mathrm{d}\alpha\, \mathrm{d}\beta\, \mathrm{d}\gamma$ is transformed into $\boldsymbol{q}$ coordinates (Warren 1969),

$$\mathrm{d}\alpha\, \mathrm{d}\beta\, \mathrm{d}\gamma = \left(\frac{\lambda}{2\pi}\right)^3 \frac{a_1 a_2 a_3}{V \sin(2\theta)} \mathrm{d}q_1\, \mathrm{d}q_2\, \mathrm{d}q_3, \tag{9}$$

where V is the unit-cell volume. a_3, the lattice parameter normal to the plane is not defined in the two-dimensional situation of fig. 2, so we substitute the unit-cell area, $\Gamma = V/a_3$. We are now ready to integrate $|A_s|^2$ defined by eq. (4),

$$\begin{aligned} E &= \left(\frac{\lambda}{2\pi}\right)^3 \frac{a_1 a_2}{\Gamma \sin(2\theta)} \frac{R^2}{\Omega} \int |A_s|^2\, \mathrm{d}q_1\, \mathrm{d}q_2\, \mathrm{d}q_3 \\ &= A_0^2 \frac{e^4}{m^2 c^4 R^2} |F|^2 \left(\frac{\lambda}{2\pi}\right)^3 \frac{a_1 a_2}{\Gamma \sin(2\theta)} \frac{R^2}{\Omega} \\ &\quad \times \int \left[\frac{\sin(\frac{1}{2} N_1 q_1 a_1)}{\sin(\frac{1}{2} q_1 a_1)}\right]^2 \left[\frac{\sin(\frac{1}{2} N_2 q_2 a_2)}{\sin(\frac{1}{2} q_2 a_2)}\right]^2 \mathrm{d}q_1\, \mathrm{d}q_2\, \mathrm{d}q_3 \\ &= \frac{A_0^2 e^4 |F|^2 \lambda^3}{m^2 c^4 \Gamma \Omega \sin(2\theta)} N_1 N_2 \frac{\Delta Q_3}{2\pi}. \end{aligned} \tag{10}$$

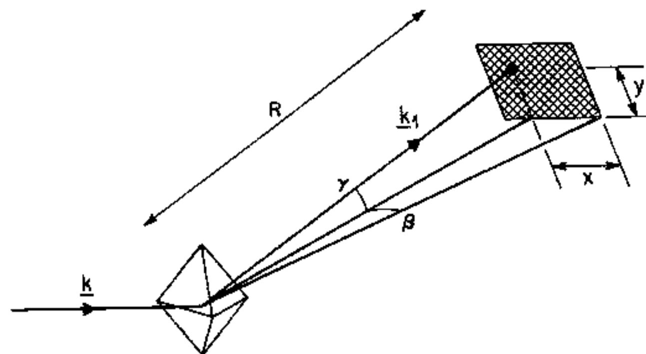

Fig. 3. Perspective drawing of the assumed experimental geometry for determination of integrated intensities. The shaded object is the rectangular slit in front of the detector, a distance R from the sample.

This is proportional to $N_1 N_2$, the number of scattering atoms in the sample, as expected. In contrast to the three-dimensional case, we find that the integrated intensity depends upon an instrumental parameter, ΔQ_3. ΔQ_3 is the length of diffraction rod (measured in reciprocal Ångstrom units) that is allowed to pass the exit slit. In general, ΔQ_3 will vary with the instrumental setting and so change from one measurement to the next. Fortunately, in the glancing incidence geometry that is commonly used (see below), the direction $\hat{q}_3$ is perpendicular to the scattering plane and ΔQ_3 is then a constant related to the size of the exit slit in the direction of the rod, L,

$$(\Delta Q_3)_{\mathrm{GI}} = \frac{2\pi}{\lambda}\frac{L}{R}. \tag{11}$$

2.3. Counting rate

Although it is the integrated intensity E that is the usual object of crystallographic measurements, it is instructive to calculate peak counting rates as well so that we can determine the feasibility of monolayer diffraction experiments. Since the resolution of a synchrotron radiation experiment is usually finer than the mosaic spread, $\Delta\omega$, of a typical crystal, the latter number determines the peak counting rate, R_{GI}, in a glancing incidence experiment,

$$R_{\mathrm{GI}} = E\frac{\Omega}{\Delta\omega} = \frac{A_0^2 e^4 |F|^2 \lambda^2}{m^2 c^4 \Gamma \sin(2\theta)} N_1 N_2 \frac{L}{R\Delta\omega}. \tag{12}$$

Typical instrumental parameters for the focussed wiggler beamline VII-2 at Stanford Synchrotron Radiation Laboratory (SSRL) with 3 GeV and 50 mA are (Moncton and Brown 1983)

$$A_0^2 = 0.5 \times 10^{13}\ \mathrm{s}^{-1}/8\ \mathrm{mm}^2, \quad \lambda = 1.7\ \text{Å},$$

$$L = 5\ \mathrm{mm}, \quad R = 500\ \mathrm{mm}, \quad e^4/m^2c^4 = 8 \times 10^{-24}\ \mathrm{mm}^2.$$

Sample parameters for a close-packed (111) monolayer of gold, assuming a typically observed mosaic spread for bulk gold crystals, are

$$|F| = 79, \quad N_1 = N_2 = 2\ \mathrm{mm}/2.9\ \text{Å} = 7 \times 10^6,$$

$$\Gamma = (2.9)^2\sqrt{\tfrac{3}{2}} = 7.3\ \text{Å}^2, \quad \Delta\omega = 0.5° = 9\ \mathrm{mrad}.$$

This yields 7×10^5 photons/s in the diffracted beam. Clearly, such experiments are practical.

Having obtained a general formula for the experimental counting rate, we can immediately see how it depends upon system parameters. It scales linearly with incident intensity, so a high-power rotating-anode source with graphite optics would give a smaller signal by ~200 (Moncton and Brown 1983), unless the resolution were to become broader than the assumed mosaic spread of 0.5°. This change alone would still leave a viable experiment. Lighter elements than gold would diffract in proportion to Z^2; a signal from silicon would, therefore, be weaker by a factor of 30. This factor could probably be regained by the improvement in sample mosaic spread if the silicon monolayer were as well-ordered as bulk silicon usually is. The steepest dependence of

eq. (12), however, is on unit cell size, a, which appears twice in the value of N^2 when the illuminated area is constant and twice in Γ, giving a total dependence of a^{-4}. A Si(111)7 × 7 monolayer structure would, therefore, contribute a factor of $7^4 = 2401$ per atom less than a Si(111)1 × 1 layer. This is partly cancelled by changes in $|F|^2$ when there is more than one atom per unit cell, but in order to solve a structure it is necessary to measure $|F|$ accurately enough to see the contribution of a single atom per unit cell.

We have determined that a monolayer of ordered material gives rise to a reasonably strong diffraction signal when synchrotron radiation is used. The real situation of interest to surface crystallography is a monolayer on the surface of a bulk crystal. Problems that have attracted attention are those of reconstructed surfaces and adsorbed layers where the surface layer or layers have a unique structure with different translational symmetry from the bulk. The diffraction from the surface then appears in totally new places in reciprocal space, easily distinguished from the bulk diffraction. The bulk does, however, contribute in two important ways: as an unavoidable background, and in the form of 'crystal truncation rods'.

2.4. *Background*

The reason the bulk background can be a problem is that there are so many more layers of bulk than surface. Thermal diffuse scattering (TDS) is the largest component (Warren 1969), but, for shorter-wavelength X-rays, Compton scattering can contribute too. TDS can be reduced in three ways experimentally. Firstly, the sample may be cooled to low temperature to reduce the thermal motions; this is not, however, always practical. Secondly, the use of glancing-incidence and/or glancing-exit diffraction geometries (see below) reduces the penetration into the bulk and hence the bulk background contribution. The most effective method, though, is the use of high-resolution techniques which are particularly appropriate to synchrotron-radiation facilities. By reducing the volume of reciprocal space sampled, the background is reduced in proportion, while the signal is unchanged, providing, of course, that the sample is sufficiently well-ordered. It is for this reason that it is desirable to use crystal analysers in surface-diffraction experiments.

Typical background levels observed in practice (Robinson 1986) for platinum single crystals with modest resolution (0.4° graphite monochromator and analyzer) are approximately equal to the diffraction signal from a monolayer for large incidence angle (45°) and considerably lower when glancing incidence is used. In situations where high resolution and glancing incidence are used, background from the sample can be so low as to be undetectable and is dominated instead by stray radiation and detector dark counts (0.1 counts/s typically for NaI scintillation detectors). An additional problem, especially in attempts to use anomalous-diffraction methods, is bulk fluorescence which may be hard to remove near to absorption edges, particularly if no analyzer is used.

2.5. *Crystal truncation rods*

Crystal truncation rods are two-dimensional diffraction features that arise from bulk crystals that terminate with a sharp boundary (Robinson 1986). They have many

features in common with diffraction rods from monolayers, so must always be considered in experiments to determine the structure of unique layers at crystal surfaces. A bulk crystal consisting of N_3 layers of $N_1 \times N_2$ unit cells has a total diffraction intensity analogous to eq. (4),

$$I_b(q) = A_0^2 \frac{e^4}{m^2c^4R^2}|F|^2 \frac{\sin^2(\frac{1}{2}N_1q_1a_1)\sin^2(\frac{1}{2}N_2q_2a_2)\sin^2(\frac{1}{2}N_3q_3a_3)}{\sin^2(\frac{1}{2}q_1a_1)\sin^2(\frac{1}{2}q_2a_2)\sin^2(\frac{1}{2}q_3a_3)}. \tag{13}$$

If we satisfy the two in-plane Laue conditions as in eq. (6) and consider the dependence of the bulk contribution on q_3, namely the component of the momentum transfer normal to the crystal face under examination. When $q_3a_3 = 2\pi l$ is satisfied as well, we have a bulk Bragg peak; but when $q_3a_3 \neq 2\pi l$, we can take an average value for $\sin^2(\frac{1}{2}N_3q_3a_3)$ by assuming N_3a_3 is large compared with the resolution length,

$$I_b\left(\frac{2\pi h}{a_1}, \frac{2\pi k}{a_2}, q_3\right) = A_0^2 \frac{e^4}{m^2c^4R^2}|F|^2N_1^2N_2^2 \frac{1}{2\sin^2(\frac{1}{2}q_3a_3)}. \tag{14}$$

Comparing eq. (14) with eq. (7), we see that the bulk truncation and unique monolayer contributions are of the same order of magnitude. The bulk truncation rods have the characteristic $[\sin(\frac{1}{2}q_3a_3)]^{-2}$ shape, while monolayer diffraction rods are flat, although surface structures more than one layer thick will generally have modulations as a function of q_3. Examples of crystal truncation rods are shown in figs. 4 and 5.

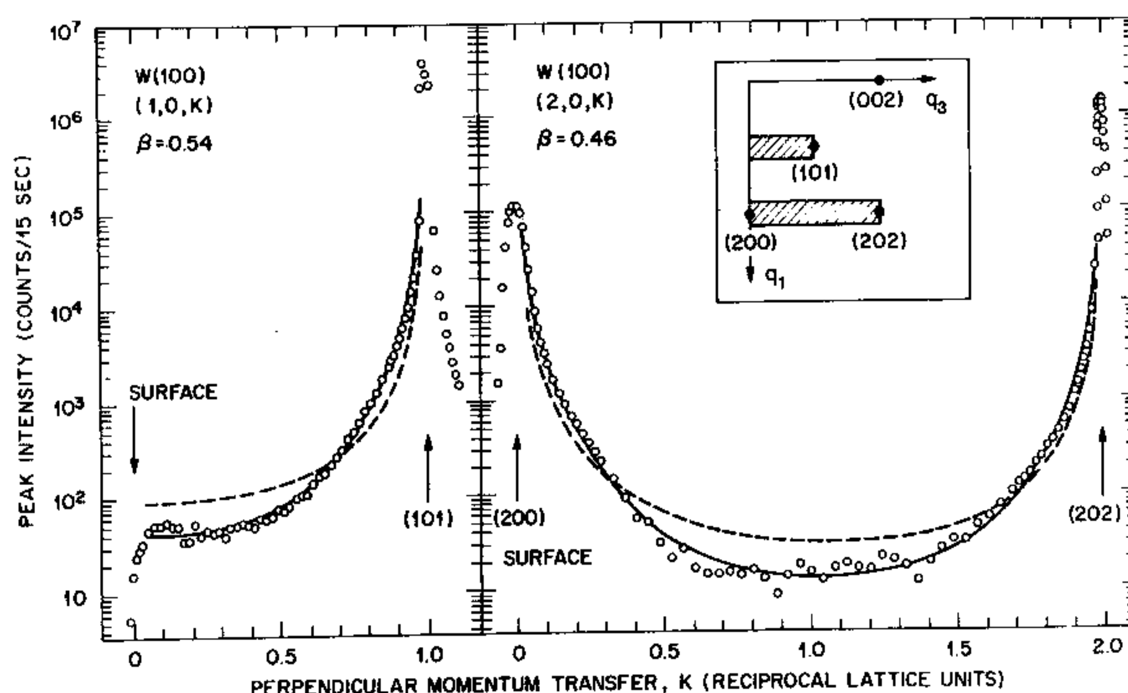

Fig. 4. Crystal truncation rods for a W(100) surface in ultrahigh vacuum (UHV) (Robinson 1986). Bars in the reciprocal-space diagram in the inset show the range of the two scans shown. q_3 is perpendicular to the surface, q_2 parallel; indexing is with bulk Miller indices. Measurements were made with a 60 kW rotating-anode source, graphite resolution and a four-circle diffractometer in the symmetric $\omega = 0$ mode. The dashed line is an attempt to fit the ideal truncation rod profile of eq. (14); the solid lines are independent fits of rough rod profiles, eq. (15), with $\beta = 0.54 \pm 0.15$ and 0.46 ± 0.10, respectively.

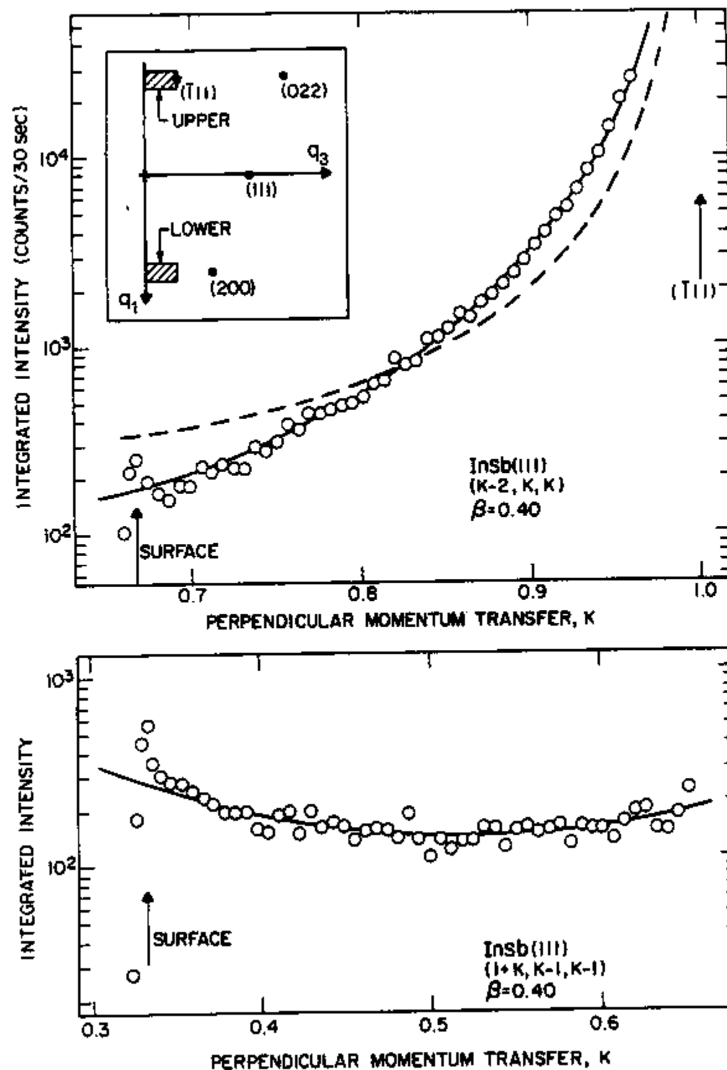

Fig. 5. Crystal truncation rods for an InSb(111) surface in UHV (Robinson 1986). Measurements were made at Hamburger Synchrotronstrahlungslabor (HASYLAB) with bending-magnet synchrotron radiation on the D4 line, double Ge(111) monochromator, plane Au filter mirror, horizontal-scattering geometry and linear-position sensitive detector. Each intensity point is integrated over sample orientation as in eq. (12). Fits are as in fig. 4 with $\beta = 0.40 \pm 0.05$.

2.6. Reconstructed surfaces

Low-energy electron diffraction (LEED) (van Hove and Tong 1979) studies have shown that clean reconstructed surfaces and adsorbate systems frequently show periodicities that are integer multiples of the bulk period. An "$n \times m$" structure repeats every n bulk spacings in one surface direction and every m spacings in the other. The reciprocal lattice, therefore, has diffraction rods at fractional order positions $(i/n, j/m)$. The overlap between surface layer and bulk truncation scattering occurs at integer order positions, where the two amplitudes will add together. This interference can provide useful information about the registry of the surface and the bulk. The possible use of this interference in crystallographic phase determination is also discussed in sect. 6.5.

2.7. Surface roughness

Surface roughness is found to be important in understanding the shapes of crystal truncation rods, such as figs. 4 and 5 (Robinson 1986). To understand why this is important, it is useful to consider the effect of crystal truncation as the multiplication of an infinite lattice by a step function at the surface. The diffraction pattern is then a convolution of a reciprocal lattice of infinitely sharp δ-functions with the Fourier transform of a step function, $1/q$. This gives a $1/(\Delta q_3)^2$ smearing of each Bragg point in the direction perpendicular to the surface, which produces the overall $[\sin(\frac{1}{2}q_3 a_3)]^{-2}$ dependence of eq. (14). If, in place of a step function, some broader probability distribution is used to represent the termination of a rough surface, the Fourier transform will be sharper than $1/q$, and the resulting lineshape will be more concentrated near the bulk Bragg peaks and away from the zone centre. The functional form used to fit data of figs. 4 and 5 is

$$I_R = I_0 \frac{(1-\beta)^2}{1+\beta^2-2\beta\cos(q_3 a_3)} \frac{1}{\sin^2(\frac{1}{2}q_3 a_3)}, \tag{15}$$

with $0 < \beta < 1$ representing the roughness. This was derived for a particular model of surface roughness (Robinson 1986) in which a surface with $\beta = 0$ is perfectly flat and with $\beta = 1$ is infinitely rough.

3. Experimental techniques

The four-circle diffractometer is a widely used general purpose instrument for measuring X-ray diffraction intensities in three dimensions of reciprocal space. It is particularly well-suited to synchrotron-radiation applications when the principal axis is horizontal and the scattering plane vertical. This is because the long direction of the resolution function of the source is always exactly aligned with that of the analyzer. Other experimental configurations have been used successfully, particularly to take advantage of parallel detection, and they will also be discussed.

3.1. Four-circle diffractometer

Figure 6 defines the four angles of the four-circle machine (Busing and Levy 1967). The scattering angle from the direct beam to the detector is defined as (2θ). All four axes are concentric to within 10 μm and should be accurate to 0.005° and movable in steps of 0.001°, except for χ which may be a little less accurate.

The transformation from a general position in reciprocal space $\{q_1, q_2, q_3\}$ to diffractometer setting $\{2\theta, \theta, \chi, \phi\}$ is nonlinear and depends on the alignment of the sample on the ϕ table. Sometimes, a crystal may be prealigned with a principal zone exactly parallel to the ϕ-axis by means of a goniometer head, but this is not always possible. It is common to use an on-line computer to perform the non-linear transformation and set the angles by means of stepping motors. In this way, arbitrary straight lines may be scanned in reciprocal space for easy interpretation. Figure 4 is an example of this: all four motors move between every point of these scans. Since the

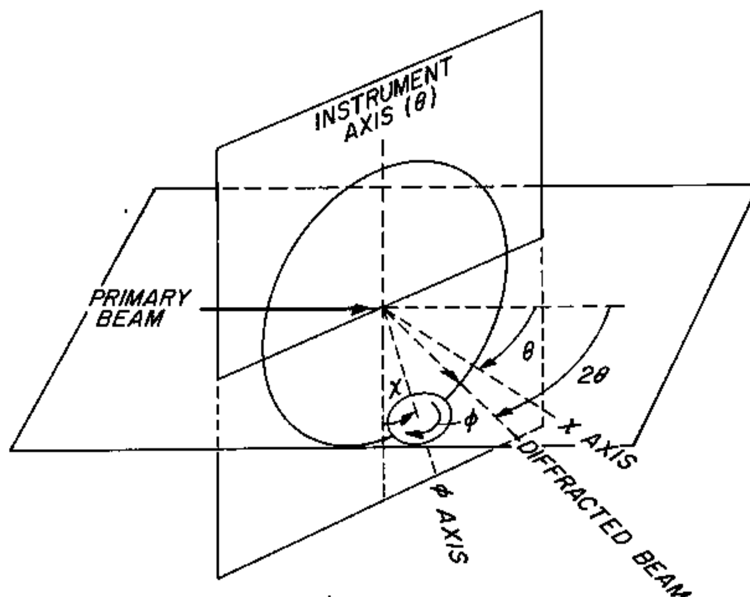

Fig. 6. Angle conventions for a four-circle diffractometer (adapted from Busing and Levy 1967).

transformation from three coordinates to four angles is underconstrained a *convention* must be specified to constrain the calculation. Examples of conventions in use are:

(i) symmetric or "$\omega = 0$" mode: $\theta = \frac{1}{2}(2\theta)$ (Busing and Levy 1967, Fleming 1985, Braslau 1987);

(ii) constant angle of incidence on sample face (Mochrie 1988, Vlieg et al. 1987a);

(iii) constant angle of exit from sample face (Mochrie 1988, Vlieg et al. 1987a);

(iv) angle of incidence = angle of exit (Robinson 1989);

(v) ϕ = constant, or θ = constant mode (Fleming 1985, Braslau 1987);

(vi) "two-circle" mode: ϕ = constant, χ = constant (Fleming 1985);

The last of these is overconstrained and can only access one zone of reciprocal space at a time.

The constraint problem in four-circle diffractometry is an important part of experimental design. It can be used to avoid "black angles" that would collide parts of the diffractometer or lead to obstruction of one or other of the beams. Since the extra degree of freedom is a rotation of the sample about the diffraction vector, $\boldsymbol{q}$, it can also be used to select 3-beam diffraction conditions (Post 1979) or to choose an arbitrary incident or exit angle. The latter requires (Vlieg et al. 1987a, Mochrie 1988, Robinson 1989) independent definitions of the crystal and surface orientations.

3.2. Use of synchrotron radiation

The choice of beamline and X-ray optics for surface crystallography with synchrotron radiation is fairly flexible. The requirements are for a high incident flux (A_0^2) and high resolution in the plane of the surface, ($\Delta q_{\parallel}$). Out of plane resolution ($\Delta q_{\perp}$) is *not* needed because surface diffraction is diffuse in that direction; an exception to this rule is the detailed study of total reflection (see sect. 3.5), but this is not usually needed for crystallographic work. Energy tunability is desirable to allow the use of anomalous

scattering, but narrow bandwidth ($\Delta E/E$) is not required except to the extent that it must not significantly affect resolution through dispersion.

A prototypical design for an X-ray diffraction beamline is that of VII-2 at Stanford Synchrotron Radiation Laboratory (SSRL) (Moncton and Brown 1983). Many variations of this design have appeared since. There are two basic optical components: a toroidal focussing mirror and a double crystal monochromator. The toroidal mirror (Howell and Horowitz 1975) is a convenient way of collecting several milliradians of synchrotron radiation. It is illuminated at a sufficiently glancing angle for total reflection to take place in order to achieve point-to-point imaging of the source. As storage ring emittances have been made progressively smaller the limitations of manufacture of such mirrors are becoming apparent: it may turn out that image sizes smaller than ~ 1 mm (FWHM) may never be achieved. To take full advantage of low-emittance storage rings, a substitute for the mirror may have to be found.

The second optical component of the "standard" beamline is the double crystal monochromator. This is usually placed as close to the sample position as possible because crystal heating can result in small angular shifts of the exit beam. It can be placed in front of the mirror to achieve narrow bandwidth and to reduce thermal problems in the mirror, but this causes additional mirror-alignment difficulties instead. Because the monochromatic flux delivered to the sample is directly proportional to the bandwidth, it is desirable to make this fairly large. Here, we are limited by the rocking-curve widths ($\Delta\omega$) of available perfect single-crystalline materials. Ge(111) is the best choice among readily available materials, with $\Delta\omega = 0.008°$ resulting in $\Delta E/E = 10^{-3}$ at $E = 15$ kV or 5×10^{-4} at $E = 7.5$ kV. To increase the bandwidth (hence throughput) still further by a factor of 2–3, asymmetrically cut Ge(111) can be used at an incidence angle of $\sim 2°$ instead of 15° (7.5 kV); although this reduces the monochromator tuning range, it also improves the distribution of heat on the first crystal (Kikuta and Kohra 1970).

3.3. Resolution function

The four-circle diffractometer is constructed to have a scattering plane, in which the detector moves, that is fixed in space as shown in fig. 6. The overall resolution of the instrument is thus determined primarily by resolution within the plane, with only second-order coupling out-of-plane, due to curvature of the Ewald sphere. For this reason, the scattering plane is oriented *vertically* (with the 2θ-axis horizontal) to match the narrow vertical opening angle of synchrotron radiation. The monochromator and analyzer crystals scatter vertically for the same reason. Resolution in the horizontal direction is degraded as much as possible, by use of wide apertures, to maximize intensity. Aberrations in the mirror, which couple vertical and horizontal directions, limit the maximum horizontal collection angle to about 5 mrad (Howell and Horowitz 1975); smaller collection angles must be used when resolution needs to be pushed to its limit (Moncton and Brown 1983). The result of these optimization considerations is a highly asymmetric resolution function. We estimate the size of the resolution function in the three principal directions $\Delta q_{\parallel}$ (parallel to q), Δq_{T} (perpendicular to q, in-plane) and $\Delta q_{\perp}$ (out of plane) using the construction of fig. 7.

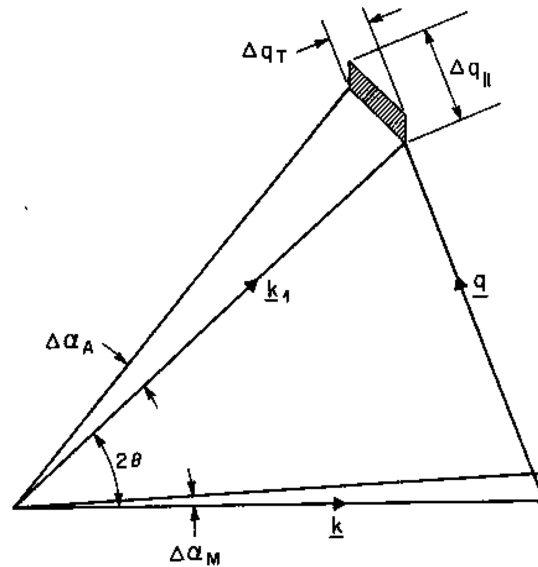

Fig. 7. Construction of idealized in-plane resolution function (shaded).

We neglect the effects of dispersion, although they can be important (Moncton and Brown 1983), and assume that the resolution is dominated by the rocking-curve widths of the monochromator, $\Delta\alpha_M$, and analyzer, $\Delta\alpha_A$, and by the horizontal acceptance of the mirror, $\Delta\beta$. Referring to fig. 7,

$$\Delta q_{\parallel} = k(\Delta\alpha_M + \Delta\alpha_A)\cos[\tfrac{1}{2}(2\theta)],$$
$$\Delta q_T = k(\Delta\alpha_M + \Delta\alpha_A)\sin[\tfrac{1}{2}(2\theta)],$$
$$\Delta q_{\perp} = k\Delta\beta. \tag{16}$$

Typical numbers are $\Delta\alpha_M = \Delta\alpha_A = 0.008°$ and $\Delta\beta = 5$ mrad, giving for 7.5 kV X-ray energy:

$$\Delta q_{\parallel} = 10^{-3}\cos[\tfrac{1}{2}(2\theta)]\ \text{Å}^{-1},$$
$$\Delta q_T = 10^{-3}\sin[\tfrac{1}{2}(2\theta)]\ \text{Å}^{-1},$$
$$\Delta q_{\perp} = 0.02\ \text{Å}^{-1}. \tag{17}$$

This assumes a narrow exit slit in the out-of-plane direction. If a wide slit is used in the geometry of fig. 3, then $\Delta q_{\perp}$ is no longer limited by the mirror aperture so is given by eq. (11) and may be as large as 0.1 Å^{-1}.

3.4. Glancing-incidence geometry

The asymmetry of the resolution function, which exceeds 20 : 1 in the case above, is the major consideration in the choice of scattering geometry used in surface crystallography. Recalling that the observed intensity at a point of reciprocal space is the convolution of the two-dimensional diffraction rod with the instrumental response, we see that this is maximized when the diffuse direction of the diffraction, q_3 in the notation above, is aligned with the long direction of the resolution function, $\Delta q_{\perp}$. To

achieve this, the incident and exit beams must graze across the physical surface of the crystal. It is, therefore, called the "glancing-incidence" diffraction geometry, and is shown in fig. 8. The small angles subtended by the two beams with the surface are denoted α and β as shown.

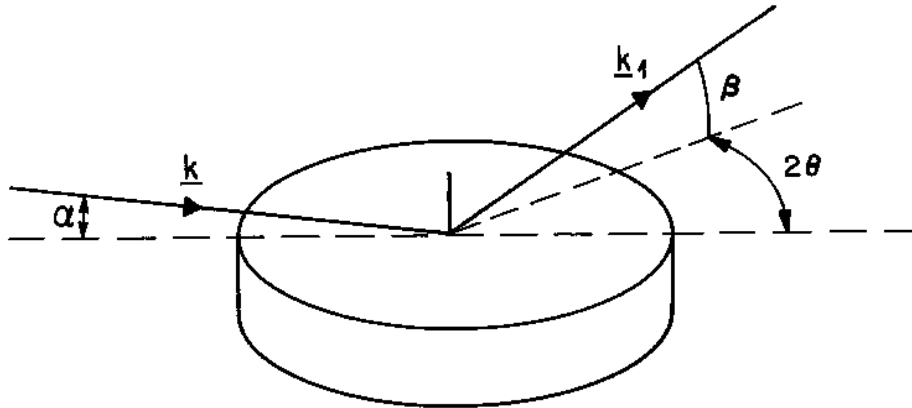

Fig. 8. Directions of beams and definition of angles for the glancing-incidence X-ray diffraction geometry.

3.5. *Total external reflection*

Because of the small angles of incidence involved with the glancing-incidence geometry, it is necessary to consider the effects of *refraction* at the surface. The refractive index, n, of a solid at X-ray wavelengths is less than unity (James 1955),

$$n = 1 - \frac{\lambda^2 e^2 F(0)}{2\pi m c^2 V}, \tag{18}$$

where $F(0)$ is the structure factor given by eq. (3), evaluated at $q = 0$, and V is the unit-cell volume. The departure from unity is thus directly proportional to the density of the material and is of the order of a few parts per million. Because n is less than one, an X-ray incident on a crystal face at a sufficiently small angle undergoes *total external reflection.* The reflectivity coefficient of a dielectric boundary as a function of angle of incidence, α, is given classically by the Fresnel law (Born and Wolf 1975),

$$\mathscr{R} = \left| \frac{\sin\alpha - \sqrt{n^2 - \cos^2\alpha}}{\sin\alpha + \sqrt{n^2 - \cos^2\alpha}} \right|^2. \tag{19}$$

Total external reflection occurs when the reflectivity is unity. This happens whenever α is less than a critical angle, α_c, given by

$$\cos\alpha_c = n, \tag{20}$$

where α_c is in the range $0.1° < \alpha_c < 0.6°$ for most materials for X-ray wavelengths. The reflectivity falls off rapidly as α^{-4} when $\alpha \gg \alpha_c$.

We can also determine the electric field strength just inside the crystal face by considering the transmission coefficient of the dielectric boundary (Born and Wolf

1975),

$$\mathscr{T} = \left| \frac{2 \sin \alpha}{\sin \alpha + \sqrt{n^2 - \cos^2 \alpha}} \right|^2 . \tag{21}$$

This coefficient tends to unity for large angles of incidence $\alpha \gg \alpha_c$. When $\alpha < \alpha_c$, the transmitted wave does not propagate but the field strength *at the surface* is still given by eq. (21), and the diffracted intensity from the atoms in the surface layer is proportional to $\mathscr{T}$. The signal is, therefore, enhanced by a factor of 4 when the incident ray approaches at exactly the critical angle, α_c. The diffracted beam experiences refraction in exactly the same way, so that a second factor of 4 may be obtained when the angle of exit from the surface, β, is equal to α_c. More detailed consideration of the theory of diffraction under total external-reflection conditions (Vineyard 1982, Dietrich and Wagner 1984) and of dynamical effects (Kishino and Kohra 1971, Afanas'ev and Melkonyan 1983, Cowan 1985) are beyond the scope of this chapter.

Experimental verification of signal enhancement due to total external reflection is shown in figs. 9 and 10. The incidence angle, α, is varied in fig. 9 and the ω-integrated surface diffraction intensity is followed. The collimation of the incident beam is very tight so as not to broaden the response, but a wide exit slit is used. In fig. 10 the surface diffraction intensity is plotted as a function of exit angle from the surface, β. In both cases, a theoretical curve is superimposed which is obtained by convolving eq. (21) with the known distribution of surface normals, as measured by reflectivity. No parameters were adjusted, yet the agreement is good. Observed enhancements are 2.8 in α and 2.65 in β, which fall short of the ideal value of 4.0 because of the smearing. Other measurements of diffraction under total external-reflection conditions are in the literature (Golovin and Imamov 1984, Imamov et al. 1983).

In practice, however, the enhancement of intensity by total external reflection (of up

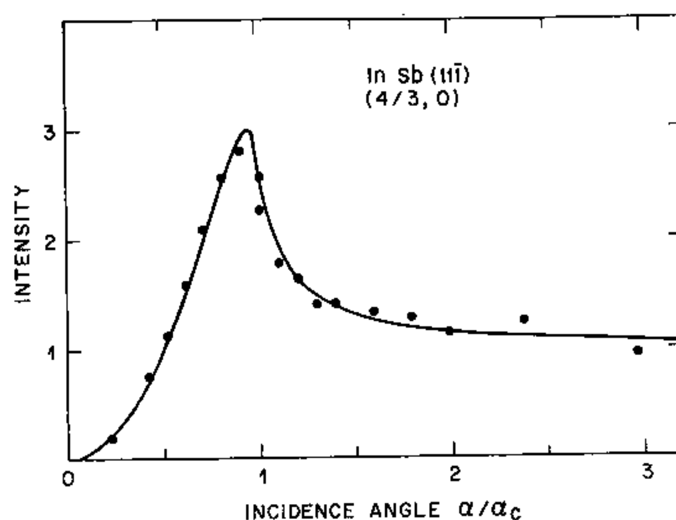

Fig. 9. Surface diffraction intensity from a clean InSb($\bar{1}$11) surface in UHV as a function of incidence angle, α. Each point is integrated over sample orientation angle ω. The $(\frac{4}{3}, 0)$ Bragg reflection arises from the 3×3 reconstruction of this surface, which is confined to the topmost layers of the crystal. The critical angle $\alpha_c = 0.25°$ at $\lambda = 1.2$ Å (Feidenhans'l et al. 1985).

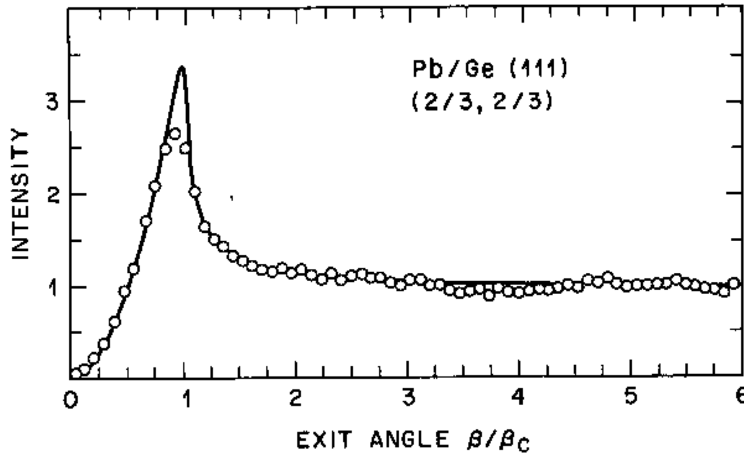

Fig. 10. Surface-diffraction intensity from 0.6 monolayers of Pb on a Ge(111) surface as a function of exit angle from the surface, β, corresponding to a distance along a position sensitive detector. Each point is ω-integrated. The $(\frac{2}{3}, \frac{2}{3})$ reflection shown is unique to the Pb monolayer which forms a crystalline $\sqrt{3} \times \sqrt{3}$ structure on Ge(111) (Feidenhans'l 1986).

to a factor of 16) is not particularly useful in crystallographic work because the range of angles α and β over which the effect is seen is so small. Figures 9 and 10 show significant enhancement over a range of 20% of α_c. Since α_c is typically 0.3° or 5 mrad, this would not allow the full horizontal aperture of our prototypical beamline to be collected inside this window. With optimal choice of α, the net enhancement would be only a factor of 1.8. The situation is worse for β since it is advantageous to collect several degrees of exit angle in a parallel fashion as mentioned above; the enhancement in β might then be only a factor of 1.1. More important is the concern that reproducibility of intensity data may also be compromised by unwanted variations of α and β from one reflection to another, or else by variations of the distribution of surface normals (an inevitable consequence of crystal polishing) from one azimuth to another. All things considered, it is often preferable to work with α and β both sufficiently larger than α_c that measurements are not affected by refraction.

3.6. Background in glancing incidence

The background, upon which a surface-diffraction signal sits, also depends strongly upon incidence and exit angles. Assuming that the main contribution comes from the bulk, we can use measurements of bulk fluorescence (Becker et al. 1983) as a good estimate of field strength (from the Fresnel theory (Born and Wolf 1975)) times the penetration depth. This should correspond directly to the angle dependence of background level in a diffraction experiment. Detailed measurements of bulk fluorescence as a function of incidence and exit angle are shown in fig. 11 for Ge. It is clear that keeping either α or β close to or less than α_c results in an enormous reduction of background, which arises mainly by restriction of penetration into the bulk or limited access by the bulk to the detector. This is the second advantage of the glancing-incidence geometry. As mentioned above, background levels are not

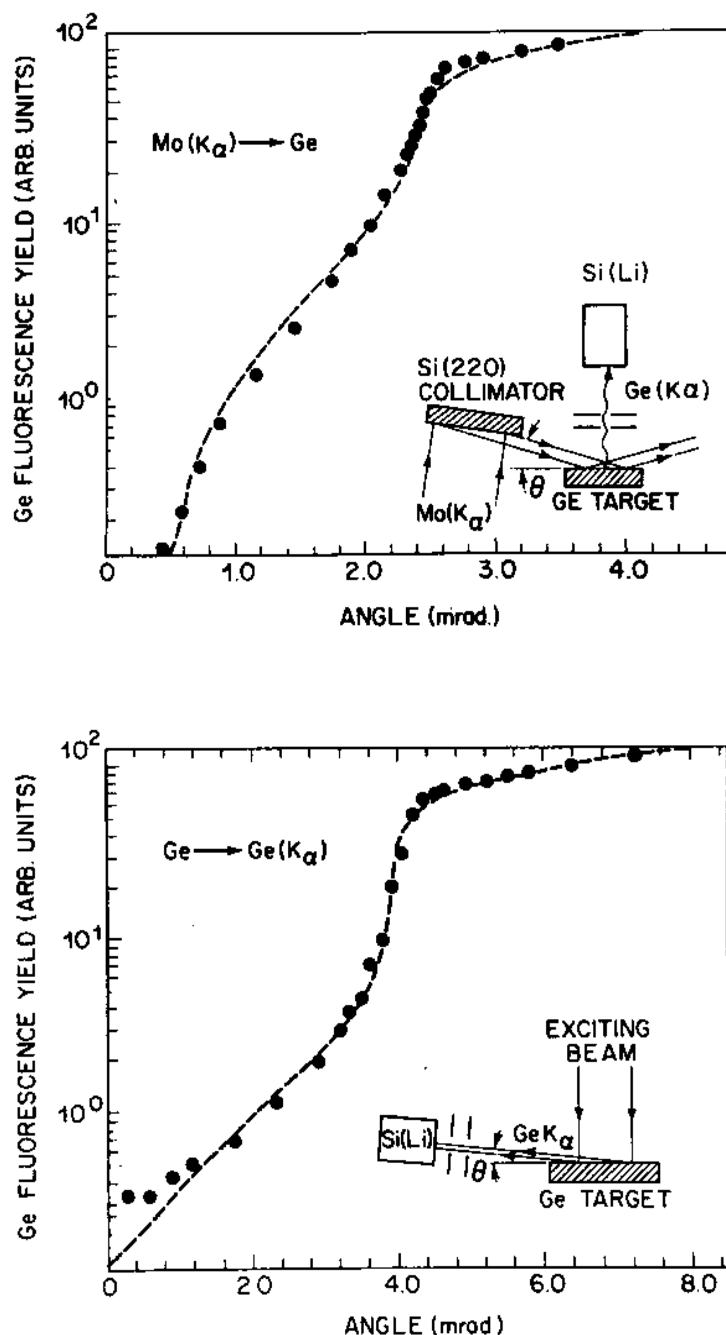

Fig. 11. Bulk fluorescence of a flat polycrystalline Ge sample as a function of (a) incidence angle, α, and (b) exit angle, β (Becker et al. 1983). The experimental geometry is inset. Mo Kα characteristic radiation (15 kV) is used to excite Ge K fluorescence (11 kV). The theoretical curves are from the Fresnel theory (Born and Wolf 1975).

found to be problematic in high-resolution experiments with well-ordered samples. Controlling and understanding penetration depth is very important, however, in work on amorphous or disordered thin films (Fuoss 1983) and in attempts to depth-profile layered structures (Marra et al. 1979, Marra 1981).

3.7. Methods of measurement

There is a conflict, in general, between the desire to align the resolution function parallel to the diffraction rod and the need to control the incident and exit angles carefully. This is aggravated further when three-dimensional data are wanted. Most surface-structure determinations reported to date have used relative order-to-order rod intensities, measured at some convenient height up the rod in order to satisfy the X-ray optical constraints. In general, however, 'rod profiles', showing the q_3 dependence, are needed to obtain information about structure in the non-periodic direction normal to the surface. This cannot be done without varying one or both of the angles α and β; nor can it be done without changing the alignment between the rod and the resolution function of the four-circle instrument. There is no general solution to this problem, so we will describe the experimental techniques used in different laboratories one by one.

3.7.1. Symmetric four-circle mode

Here, the sample is aligned as accurately as possible with the crystal planes of the nominal surface direction perpendicular to the ϕ-axis of the four-circle machine in fig. 6. This is achieved by adjusting the tilt of the sample until general bulk reflections superimpose exactly upon rotations of ϕ consistent with the space-group symmetry. The optical surface of the sample would not be exactly coincident with the crystal planes due to crystal miscut, but this is ignored. The diffractometer is then operated in the $\omega=0$ mode with $\theta=\frac{1}{2}(2\theta)$ described above. Here, the χ-circle is always symmetrically placed half-way between the incoming and outgoing beam directions. When $\chi=0$ the incident and exit beams would graze exactly across the surface if the crystal were perfectly aligned, but in practice one or other of them would be buried and no signal would be seen. However, if some small positive χ angle is set, then the sample face is tilted out of the scattering plane and the incidence and exit angles are given by

$$\sin\alpha=\sin\beta=\sin\chi\sin\theta. \tag{22}$$

Crystal misalignment means that one angle will be slightly smaller and the other slightly larger than this value. In practice, χ is set to have α and β sufficiently larger than α_c that refraction enhancement (which would fluctuate with ϕ) does not take place. This criterion takes care of imperfect sample alignment on the diffractometer as well. In this mode, sample azimuth is selected by ϕ; symmetry equivalent reflections differ only in their ϕ setting. Rod scans (varying q_3) are χ-scans to first order, with second-order corrections to θ and 2θ to account for changes in the length of the scattering vector. The compromise between signal to background (due to tilting of the resolution function with respect to the rod) and reproducibility (due to refraction effects), therefore, amounts to a choice of the optimum q_3, hence χ, hence α and β. This is dramatically illustrated in fig. 12a by a q_3 scan of a surface Bragg rod for a reconstructed Si(111)7 × 7 surface. The raw data drop off very fast because the peak becomes spread out parallel to the surface plane as the resolution function tilts; the integrated intensity would, of course, be conserved. The effects of resolution-function

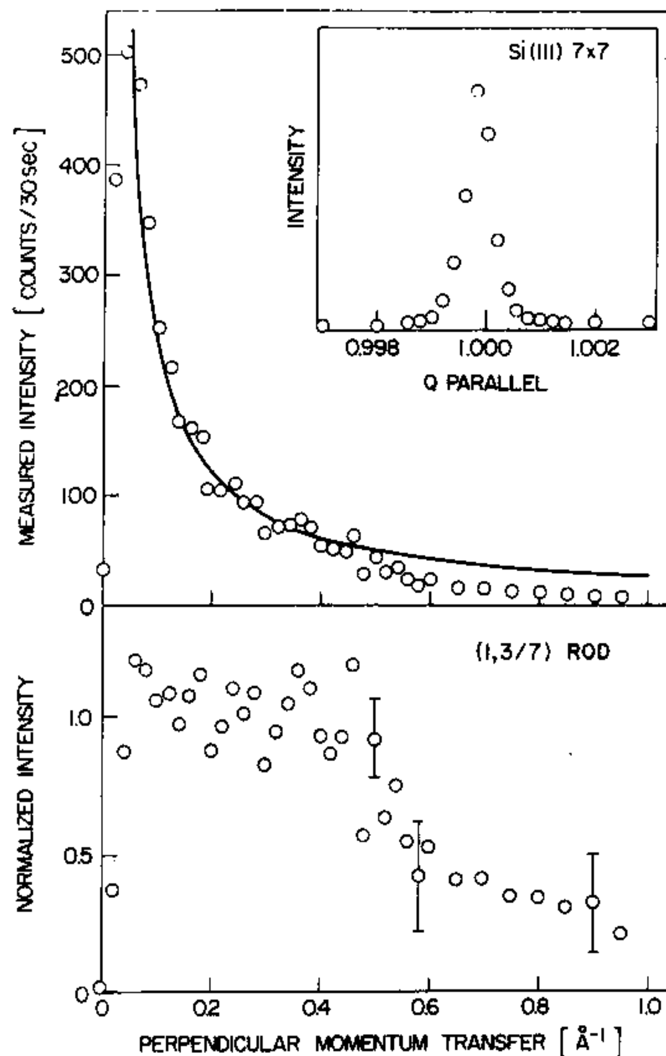

Fig. 12 (a) Rod scan for the $(1, \frac{3}{7})$ surface Bragg reflection of Si(111)7 × 7 measured in the symmetric four-circle mode. Data were measured on the focussed wiggler line VII-2 at SSRL using Ge(111) monochromators and analyser. The solid line is calculated from the known dimensions of the resolution function (Robinson 1985). (b) The same data normalized to the calculated curve.

changes are calculated as the solid curve; when these are divided out in fig. 12b, the rod assumes a slow varying shape that would be reasonable for a three-layer surface structure (Robinson 1985).

3.7.2. Other four-circle modes

More general modes of operation have been designed for the four-circle diffractometer (Mochrie 1988, Robinson 1989). These require removing the $\theta = \frac{1}{2}(2\theta)$ constraint and replacing it with a more general one. The big advantage here is that the crystal surface normal no longer has to be coincident with the ϕ-axis: alignment parameters defining that direction are input to the calculations. It naturally separates the orientation of the crystal from the orientation of the surface. This is very useful for work with miscut crystals, whether deliberately or accidentally so, and avoids the need for accurate prealignment.

Two different procedures have been derived and incorporated into control software. The method of Mochrie allows scans to be made at specific α or specific β (Mochrie 1988, Braslau 1987). The four angles are determined by $\{h, k, l, \alpha\}$ or $\{h, k, l, \beta\}$ data input. A scan at constant α, e.g., on a sample aligned to the ϕ-axis would place the χ-circle almost perpendicular to the incoming beam direction (i.e., $\theta = 0$). The alternative method is to set a constraint of $\alpha = \beta$ and specify only $\{h, k, l\}$ (Bohr et al. 1985, Fleming 1985). This keeps the incident and exit beams as far from grazing incidence as possible and so is most useful for crystallographic work (see sect. 3.5).

3.7.3. Flat two-circle mode

It is not always convenient to design an experiment that will mount on a four-circle diffractometer (see below). By using a pair of intersecting arcs instead of a χ/ϕ circle, a much larger load can be carried. The same angle definitions of fig. 6 apply, except that the range is limited to (typically)

$$80° < \chi < 100°, \quad -10° < \phi < 10°. \tag{23}$$

In order to work with glancing incidence, the surface normal is mounted perpendicular to both the ϕ- and χ-axes, so that it lies along the θ-axis when the arcs are centred ($\chi = 90°$, $\phi = 0°$). The constraints on sample alignment are exactly the same as for the symmetric four-circle mode except that ϕ and χ are always coupled motions because of the new sample orientation. The crystal azimuth is selected by θ, no longer constrained to be $\frac{1}{2}(2\theta)$, while the sample tilt is selected by the perpendicular momentum transfer, q_3, now some combination of ϕ and χ. Normally, the sample is tilted about an axis bisecting the incident and diffracted beam directions, corresponding to the symmetric mode above. The tilt setting must change from one reflection to another. It is relatively easy, however, to make rod scans at constant α or constant β by choosing a different mixture of χ and ϕ tilts (Braslau 1987).

3.7.4. Inclined two-circle mode

Instead of tilting the sample relative to the θ-axis of the two-circle diffractometer (as in fig. 6 with only θ and 2θ motions) in a way that changes from one reflection to the next, the *entire instrument* may be inclined at the chosen angle of incidence, α, to the incoming beam (Feidenhans'l 1986). Total external reflection may be used to align the optical surface of the sample exactly with the θ-axis: this is done by means of arc adjustments until the position of the reflected beam is independent of θ. Once aligned, the arcs are not moved again. The angle of incidence is then fixed also, and measurements are made using θ and 2θ. Rod scans can only be made by varying the angle of exit, β. A convenient way to achieve this is with a position-sensitive detector (PSD) placed perpendicular to the scattering plane. Because of the second-order correction to the θ and 2θ angles for positions along the rod far from $q_3 = 0$, the entire range of q_3 does not appear in the detector simultaneously. For crystallographic measurements, as mentioned above, it is the integrated intensity [eq. (10)] that is sought; this is conveniently obtained as a function of q_3 in a parallel fashion by accumulating counts in the PSD continuously as the θ angle moves at constant velocity, Ω. The data in figs. 5 and 10 were obtained in this way. The aperture in front

of the PSD must be wide enough to collect the full range of 2θ angles. Background should be very low if the incidence angle, α, is controlled carefully, but if subtraction becomes necessary it may be done point-by-point along the PSD.

The inclined two-circle method may be used with synchrotron radiation with the instrument axis either vertical or horizontal (Feidenhans'l 1986). The vertical θ-axis configuration allows a very narrow range of incidence angles onto the sample and so, below α_c, allows the background to be kept low. The range of α is limited by the vertical opening angle of radiation from the storage ring and may be as small as 0.02°, or about 10% of α_c. Sample flatness is frequently a problem in this configuration. The signal rate in this orientation is, of course, low for resolution reasons but 30 counts/s obtained for InSb(111) (Bohr et al. 1985) is certainly practical. The horizontal-axis configuration fills typically a 0.3° range of angles α giving large signals but allowing much less background control; signal rates as high as 50 000 counts/s for Pb monolayers have been obtained (Marra et al. 1982) at the same time as high in-plane resolution.

3.7.5. z-axis diffractometer

This machine combines the four degrees of freedom of the four-circle diffractometer with the direct control of incidence angle provided by the inclined two-circle geometry. The collinear θ- and 2θ-axes are horizontal but inclined to the incoming beam by a variable angle α, set by an external vertical-axis goniometer. The sample is optically aligned on the θ-axis as before, so that α is the true angle of incidence on the sample. Finally, the detector moves out of the 2θ plane by an angle β, which is the diffracted beam exit angle from the surface. Since the detector moves on three motors (α, 2θ and β) the scattering angle is compound; it is consequently very difficult to use an analyzer crystal with this instrument. The equations for mapping $\{q_1, q_2, q_3\}$ onto $\{\alpha, \theta, 2\theta, \beta\}$ have been derived (Bloch 1985) in a way analogous to those of the four-circle diffractometer (Busing and Levy 1967). Rod scans with either fixed α or fixed β are easily implemented through this formalism.

3.7.6. Five-circle diffractometer

The completely general way to control the five variables $\{h, k, l, \alpha, \beta\}$ is to add an extra diffractometer motion to make a total of five-circles. This is most easily done by the introduction of a vertical α-axis underneath the horizontal-axis four-circle machine (Gibbs et al. 1986, Vlieg et al. 1987b, Norris et al. 1987). It is also possible by the addition of an extra detector motion, perpendicular to 2θ, and again concentric with the other four angles (Liang et al. 1988a). Angle calculations for the first case have been derived and implemented (Vlieg et al. 1987a).

4. Surfaces

The simplest surfaces conceivable are the clean faces of single crystals in vacuum. These have certainly been the preoccupation of researchers working in the field of

surface X-ray crystallography so far. Many such surfaces are known to reconstruct (van Hove and Tong 1979) by adopting structures of lower symmetry than the bulk (see sect. 2.6); the energetics of how these structures are stabilized is a fundamental question of considerable interest (fqci) that still requires detailed knowledge of the atomic arrangements which surface crystallography will continue to provide. The surfaces with the next level of complexity are adsorbed layers of elements and molecules on clean surfaces; there are numerous physical and chemical problems that may be studied with careful diffraction experiments on these systems.

4.1. Ultra-high vacuum characterization

Surface scientists have developed a set of tools for characterizing these kinds of system. The fundamental prerequisite is an ultra-high vacuum (UHV) of around 10^{-10} Torr, which allows reactive surfaces to be examined for many minutes before contamination by residual gas takes place. This already places severe limitations upon experimental design, because the necessary pumps and stainless-steel vessels are very bulky and heavy. The size cannot be scaled down because the base pressure is limited by outgassing rate and conductance. To clean a surface, it is usually necessary to repeatedly "sputter and anneal" requiring an ion bombardment gun and a means of heating the sample and measuring its temperature. To determine that it is clean, some chemical analysis with sensitivity to a small fraction of a monolayer is required, usually Auger-electron spectroscopy (AES) or X-ray photoemission spectroscopy (XPS). Finally, it is wise to check that a surface is well-ordered, for which LEED is well-suited. Each of these tools is available commercially, but add to the size and weight of the sample environmental hardware. When sputter, evaporation or gas-leakage sources, deposition-rate monitors, ion gauges, and residual gas analyzers are added to the list, the total usually exceeds 200 kg of hardware.

4.2. Experimental configuration

Several schemes have been devised for combining the vacuum hardware with an X-ray diffractometer. A universal feature is that X-rays enter and leave the vacuum system through a window made of Be, around 0.5 mm thick, which is strong enough to hold vacuum; this attenuates 8 kV X-rays by about 10%. Some of these designs are shown in figs. 13–15.

4.2.1. Portable UHV cell

If a surface is stable in UHV for the entire duration of the X-ray experiment, the preparation may be performed beforehand in a large vacuum system. The sample is then transferred into a small UHV cell containing only a pump and a Be window, which mounts on the diffractometer. Once fixed to the wall of the cell, it is moved by orienting the whole assembly. The examples shown in fig. 13 are the designs of Marra (1981) at Bell Labs and of the group from Risø National Laboratory who work at HASYLAB (Feidenhans'l et al. 1985, Johnson et al. 1985).

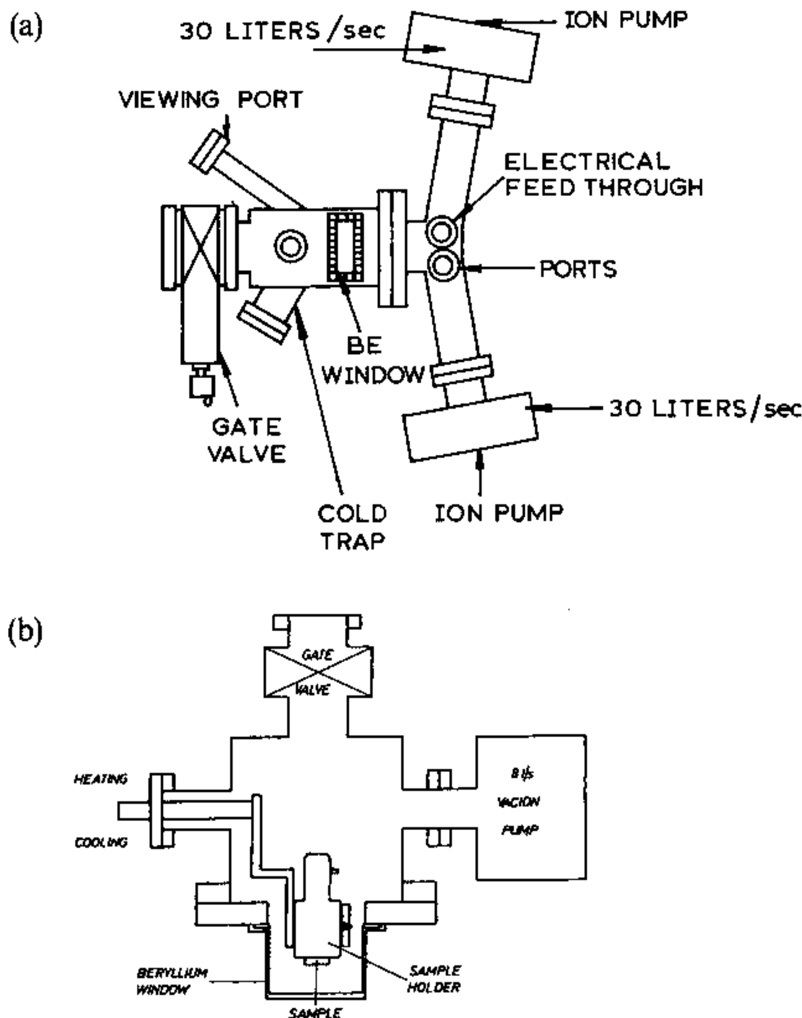

Fig. 13. Portable UHV X-ray sample cell designed by (a) Marra (1981) and (b) Johnson et al. (1985). In both cases the principal components are an ion pump, a Be window and a gate valve for connection to a mother chamber in which the samples are prepared.

4.2.2. Movable complete system

The design in fig. 14a, due to Brennan and Eisenberger (1984) at Exxon, is based on the z-axis diffractometer. Careful counterbalancing of the pump allows the diffractometer to carry the weight. The sample is fixed at the intersection of the axes, while the sputter gun and LEED/AES system slide on bellows to approach it. The 360° Be window allows X-rays to reach the sample from any angle θ. Use of a horizontal scattering geometry also facilitates carrying the weight at MIT (Chung et al. 1987) and at NEC/Photon Factory (Akimoto et al. 1989). We and other groups have built

---

Fig. 14. Movable complete UHV system designs. (a) z-axis diffractometer and UHV system built by Brennan and Eisenberger (1984) (b) System designed by the author for work on Si(111) and W(100). This is shown mounted in place on the χ/ϕ circle of a Huber four-circle diffractometer. The sample is aligned on a goniometer head which connects through bellows. Sample preparation is by electrical heating only (Altman et al. 1988).

(a)

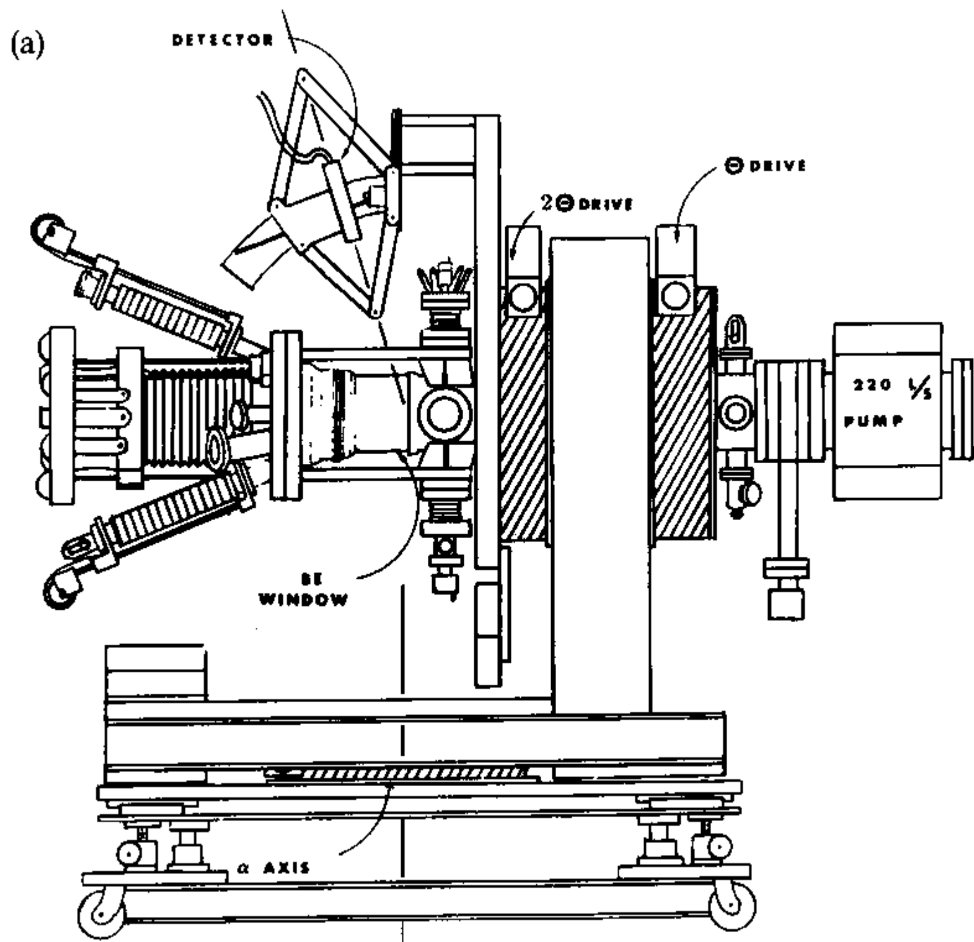

(b)

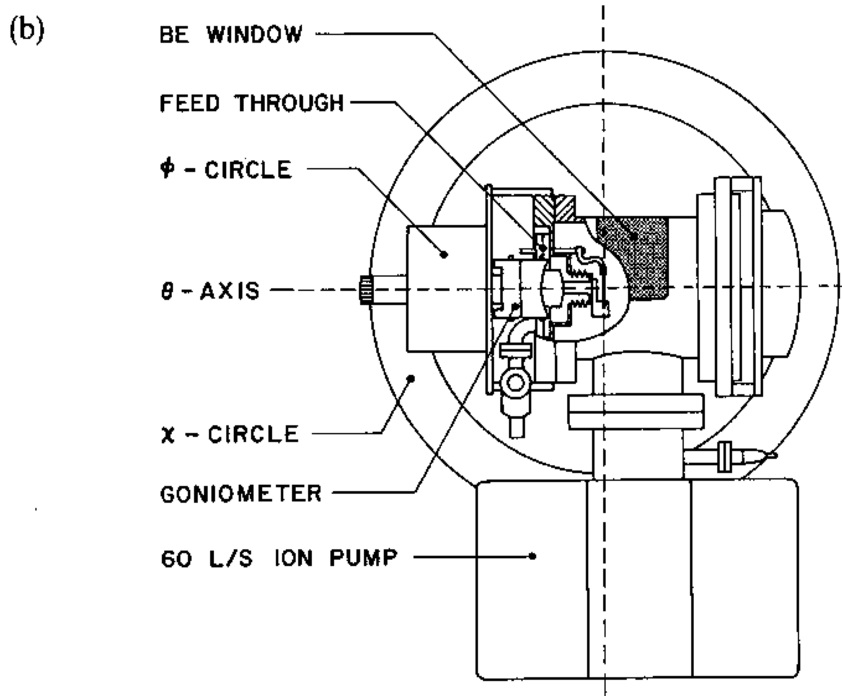

complete vacuum systems that mount directly on a standard four-circle diffractometer (Zschack et al. 1989, Robinson et al. 1986a, Altman et al. 1988, Held et al. 1987, Mochrie 1987). An example is shown in fig. 14b. This is a popular approach, because it allows experiments to be interchanged quickly. The system can be used in different places, on different beamlines (shared with other users) or with a rotating-anode source, for example.

4.2.3. Feedthrough based system

This is probably the most general approach as it places no restrictions on the weight of the vacuum system, which remains fixed; only the sample moves on the diffractometer, coupled into the vacuum by a feedthrough. The example shown in fig. 15 is our own design (Fuoss and Robinson 1984). The vacuum system and four-circle diffractometer (with limited range, $-12° < \chi < 12°$) are on opposite sides of the sample which is surrounded by a 200° Be window. The feedthrough uses bellows and a differentially pumped rotating seal. A manipulator allows the sample to be carried to the various preparation/analysis tools in the system. Variations on this design are at Brookhaven National Lab (Gibbs et al. 1986), at Daresbury/FOM (Vlieg et al. 1987b, Norris et al. 1987) at LURE (Claverie 1986, Sauvage-Simkin et al. 1989) and SUNY Stony Brook (Stephens and Eng 1988) and a very different feedthrough design is at Munich (Krebshmar and Wolf 1986).

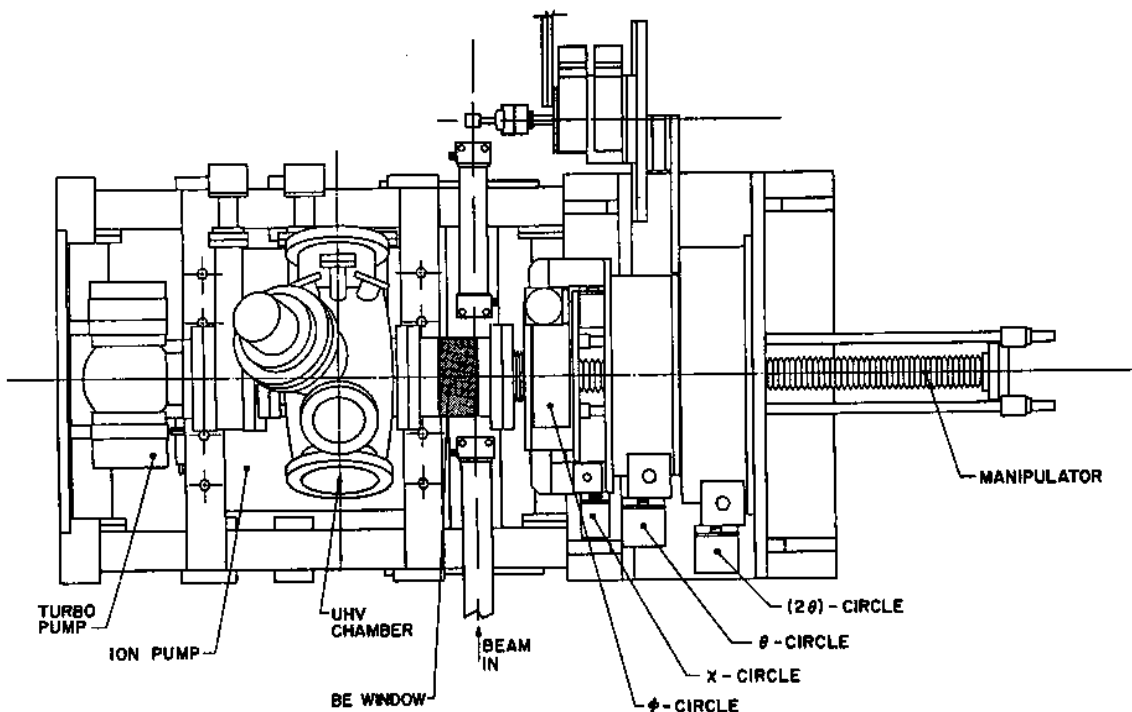

Fig. 15. Top view of a feedthrough-based surface diffractometer built by Fuoss and Robinson (1984) at AT&T Bell Labs. The instrument is for dedicated use on beamline X16A at the National Synchrotron Light Source, Brookhaven. X-rays from the beamline enter the chamber through the Be window from below, and are diffracted in a vertical plane towards the reader.

4.3. Other surfaces

Finally, it should be mentioned that not all surface-diffraction experiments require UHV. Graphite (001) surfaces are chemically inert and may be kept clean at 10^{-6} Torr for long periods. Adsorbed-monolayer experiments have been performed comfortably on a four-circle diffractometer with an apparatus in which the heaviest component is the Displex refrigerator (D'Amico et al. 1984). Work has also shown that the Si(111)7 × 7 surface periodicity can be preserved even when the clean reconstructed surface is buried with amorphous Si (Gibson et al. 1986); X-ray diffraction experiments on this kind of samples at atmospheric pressure have produced crystallographic information about solid–solid interfaces (Robinson 1987, Akimoto et al. 1987). Solid–liquid interfaces have been studied using these techniques also, during electrochemical deposition of Pb on Ag(111) (Samant et al. 1988). Crystalline monolayers have been studied on the surface of water, although little could be learned about the structure as only one Bragg peak was detected (Kjaer et al. 1987, Dutta et al. 1987).

5. Data collection

The methods of data collection and analysis have been evolving along with the experimental methods. We describe here a recommended procedure with some explanation. It is not necessarily the way in which published results have been obtained, although it corresponds most closely with more recent work.

5.1. Experimental integrated intensity

The theoretical integrated intensity is given by eq. (10) above. The experimental measurement is of a rocking curve in angle θ such as shown in fig. 16. The experimental integrated intensity, E_e, is the area of the peak minus the background. If the shape of the rocking curve was accurately known, curve fitting could be used to obtain E_e, but a good approximation is to use the area under the histogram,

$$E_e = \sum_{i=1}^{N_S} S_i - \frac{N_S}{N_B} \sum_{i=1}^{N_B} B_i, \tag{24}$$

where S_i are the number of counts in each of the N_S bins of scan points labelled "signal" and B_i are the counts in the N_B "background" bins (see fig. 16). E_e is in units of "counts". The error in E_e due to counting statistics alone is

$$\sigma_E = \left[N_S \sum_{i=1}^{N_S} S_i + \left(\frac{N_S}{N_B} \right)^2 \sum_{i=1}^{N_B} B_i \right]^{1/2}. \tag{25}$$

The choice of window, outside which points are representative of background levels, can be conservative if the scans are wide enough. Possible sources of procedural error are cutting into the edge of the peak with the window or using too coarse a step size, both of which depress the value of E_e.

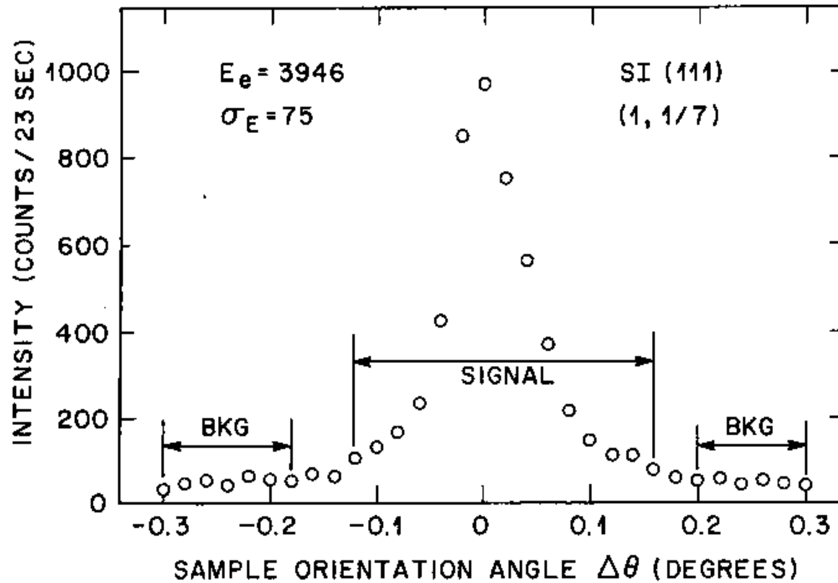

Fig. 16. Typical rocking-curve scan used to determine integrated intensity. This is of the $(1, \frac{1}{7})$ reflection of Si(111)7 × 7 measured on beamline VII-2 at SSRL (Robinson et al. 1986a).

5.2. Corrections

A series of corrections is then applied to E_e and σ_E to obtain a quantity directly proportional to $|F|^2$. Most of these are inferred directly from eq. (10). We assume that slit settings and other sensitivity parameters are unchanged throughout the experiment.

5.2.1. Angular velocity

Not all measurements are made at the same rate: weak reflections are counted for longer time to improve statistics; reflections at small 2θ can be much broader in θ by the finite domain-size effect, so may be measured with a coarser step size. The angular velocity is

$$\Omega = \frac{\text{Step size in } \theta}{\text{Total "monitor" counts per point}}. \tag{26}$$

To allow for changes in the incident beam intensity, it is conventional to use a beam monitor in place of a timer. Ω multiplies E_e.

5.2.2. Lorentz factor

In order to correct for the Lorentz factor, E_e is multiplied by $\sin(2\theta)$ as required by eq. (10).

5.2.3. Polarization factor

Synchrotron radiation is highly polarized in the horizontal plane. When the scattering plane is vertical (2θ-axis horizontal), there is no correction. When the scattering plane is horizontal (2θ-vertical), E_e is divided by $\cos^2(2\theta)$. When 2θ is close to 90°, this

factor must then be modified to include the degree of polarization of the source. When an unpolarized source, such as a rotating anode, is used, E_e is divided by $1 + \cos^2(2\theta)$. When the z-axis diffractometer is used, the correction is more complicated (Bloch 1985).

5.2.4. Area correction

If the entire face of the sample was bathed uniformly by the beam and the detector aperture was wide enough to accept radiation from the whole sample, there would be no area correction. In practice, the edges of the sample may not be well defined, often because of imperfect sample preparation. It is then desirable to define a small region in the centre of the sample by means of entrance and exit slits, cutting parallel to the face. The active region is then a parallelogram of area $L_1 L_2/\sin(2\theta)$ where L_1 and L_2 are the slit widths (typically 1 or 2 mm). E_e must, therefore, be multiplied by $\sin(2\theta)$. This correction is invalid at small 2θ when $\max(L_1, L_2)/\sin(2\theta)$ exceeds the dimension of the sample; a more detailed area correction, which depends on the shape and orientation of the sample, must then be derived.

5.2.5. Out-of-plane measurements

The area correction is modified again when out-of-phase measurements are made by tilting the sample. If χ is the angle of tilt of the sample in the diffraction plane (or the angle of inclination of the detector in the inclined 2-circle mode), the active area becomes $L_1 L_2/\sin(2\theta) \cos \chi$ (Robinson 1988).

A second correction is required if scans are made along diffraction rods because of the effects of tilting the resolution function (see sect. 3.7.1. and fig. 12). This can be compensated by measuring the radial widths which change as a function of perpendicular momentum transfer q_3, or else by calculating these from the resolution function parameters (Robinson 1988).

5.3. Statistical analysis

Once these four corrections are made, the resulting E'_e and σ'_E values are then representative of $|F|^2$, the square of the structure factor amplitude. While σ'_E is a measure of the error in E'_e due to counting statistics, it does not include systematic errors such as variations in the quality of the surface preparation and diffractometer misalignments. To measure these, it is important to take advantage of the surface symmetry by collecting several *symmetry equivalents* of each reflection; since these are made at very different angle settings and usually probe a different region of the surface, the systematic errors are represented in the variations of equivalent observations. Usually the number of equivalents sampled is too small for their standard deviation to be an accurate measure of the error, so some means of using the overall measurement statistics must be invented. The following scheme was devised by the author, but follows closely the traditional crystallographic protocols (Grant et al. 1969).

Let the n repeated measurements of a given E'_e be denoted $\{E_i, \sigma_i\}$ for $i = 1 \dots n$.

The weighted averages and standard deviation are

$$\tilde{E}=\sum_{i=1}^{n}\frac{E_i}{\sigma_i^2}\Big/\sum_{i=1}^{n}\frac{1}{\sigma_i^2},$$

$$\tilde{\sigma}=\left(\sum_{i=1}^{n}\frac{1}{\sigma_i^2}\right)^{-1/2},$$

$$s=\left(\sum_{i=1}^{n}\frac{E_i^2}{\sigma_i^2}\Big/\sum_{i=1}^{n}\frac{1}{\sigma_i^2}-\tilde{E}^2\right)^{1/2}. \tag{27}$$

We now insert an index j to label the different reflections of the data set. We assume the systematic error to be a fixed proportion, ε, of the intensity and to be measured by s_j,

$$\varepsilon=\frac{1}{N}\sum_{\tilde{E}_j>2\tilde{\sigma}_j}\frac{s_j}{\tilde{E}_j}, \tag{28}$$

where N is the number of measurements with $\tilde{E}_j>2\tilde{\sigma}_j$ included in the sum; we only include sufficiently reliable measurements in the average. The final experimental error in $\tilde{E}_j$ is now the quadrature sum of the random and systematic errors,

$$\tilde{\sigma}'_j=(\tilde{\sigma}_j^2+\varepsilon^2\tilde{E}_j^2)^{1/2}. \tag{29}$$

This formula can be used on all reflections even those measured only once which have no s_j. Reflections observed to have $\tilde{E}_j<0$ should be set to $\tilde{E}_j=0$ first.

5.4. *Quality estimates*

The $\{\tilde{E}_j, \tilde{\sigma}'_j\}$ data are now ready for analysis. It is only by carefully accounting for the errors that the uniqueness of structural information can be ascertained. It would, nevertheless, be useful to have an overall statistic for the "quality" of the measurements. Customarily in crystallography, the intensity R-factor (Stout and Jensen 1968) is used,

$$R=\frac{\sum\tilde{\sigma}'_j}{\sum\tilde{E}_j}, \tag{30}$$

often expressed as a percentage error. Alternatively, an R-factor based on $F=\sqrt{E}$, defined similarly, is used which would have about half this value. This single number can be very misleading, as it depends heavily on whether zero measurements are included or not. At present, a data-collection R-factor of 10% is fairly respectable (Bohr et al. 1985), but there is certainly room for improvement.

6. *Data analysis*

There are many excellent textbooks on the subject of crystallographic structure determination (Stout and Jensen 1968, Lipson and Cochran 1966, Buerger 1960,

Blundell and Johnson 1976), and we do not have space to mention all the available methods. Although the number of techniques is large, they are all based on the fundamental principles of wave superposition and Fourier analysis; this is because the Born approximation scattering process (valid for X-rays) is inherently linear. This is the basic reason why X-ray structural analysis is so advanced, compared with electron, ion or atom-based scattering techniques. Surface-structure analysis by LEED has made much progress in the theoretical treatment of multiple scattering (van Hove and Tong 1979), but calculations of sufficient accuracy are very time-consuming and are only practical for small unit cells. Least-squares refinement of structural models is still a very distant hope.

In principle, techniques that work in three dimensions should be valid in two dimensions, except that some of the probabilistic parameters may have to be changed. In fact, an increasing number of structural studies have incorporated full three-dimensional data by using the "rod profiles" of each two-dimensional reflection (Robinson 1983, Feidenhans'l et al. 1986b). The complete structure factor is a continuous function of the perpendicular momentum transfer, q_3, and cannot be handled by conventional crystallographic computer programs. This problem can be avoided by sampling the rods at regular intervals, Δq_3, closely spaced enough to retain all information. The calculations are then performed in the corresponding monoclinic, orthorhombic, tetragonal or hexagonal three-dimensional space group (P31m instead of p31m etc.) with a perpendicular lattice parameter of $2\pi/\Delta q_3$. It is expected that surfaces will be analyzed first in two dimensions with the later addition of partial three-dimensional data, either in the form of fractional order rod profiles, crystal truncation rods (see sect. 6.8) or by specular reflectivity (see chapter 12 by Als-Nielsen).

The reason that problems may be so conveniently divided into these steps follows from the "section–projection theorem" of Fourier transforms (Riley 1974). If $F(\boldsymbol{q})$ be the three-dimensional Fourier transform of the density, $\rho(\boldsymbol{r})$, a general statement of eq. (3) is

$$F(\boldsymbol{q}) = \int \rho(\boldsymbol{r})\, e^{i\boldsymbol{q}\cdot\boldsymbol{r}}\, d^3\boldsymbol{r}. \tag{31}$$

Consider the $q_3 = 0$ section, remembering that the surface-normal unit vector $\hat{\boldsymbol{r}}_3$ is defined orthogonal to $\hat{\boldsymbol{r}}_1$ and $\hat{\boldsymbol{r}}_2$ in fig. 2,

$$\begin{aligned} F(q_1, q_2, 0) &= \int \rho(\boldsymbol{r})\, e^{i(q_1 r_1 + q_2 r_2)} \hat{\boldsymbol{r}}_1 \cdot \hat{\boldsymbol{r}}_2 \times \hat{\boldsymbol{r}}_3\, dr_1\, dr_2\, dr_3 \\ &= \int \left[\int_{-\infty}^{\infty} \rho(\boldsymbol{r})\, dr_3 \right] e^{i(q_1 r_1 + q_2 r_2)} \hat{\boldsymbol{r}}_1 \cdot \hat{\boldsymbol{r}}_2\, dr_1\, dr_2 \\ &= \int \rho_0(r_1, r_2)\, e^{i(q_1 r_1 + q_2 r_2)} \hat{\boldsymbol{r}}_1 \cdot \hat{\boldsymbol{r}}_2\, dr_1\, dr_2. \end{aligned} \tag{32}$$

This *section* is the two-dimensional Fourier transform of the *projected* density, ρ_0, obtained by integrating the three-dimensional density over all r_3. Thus, by analyzing

the $q_3 = 0$ structure represented by the in-plane structure factor amplitudes,

$$|F_{hk}| = \left| F\left(\frac{2\pi h}{a_1}, \frac{2\pi k}{a_2}, 0\right)\right|, \tag{33}$$

we obtain the projection of the surface structure onto the surface plane. We will, henceforth, restrict our discussion of methods to the determination of ρ_0 in two dimensions.

6.1. *The phase problem*

It is because we measure only the *amplitude* of the structure factor that we cannot immediately invert eq. (31) to obtain $\rho_0(\boldsymbol{r})$. Associated with each amplitude $|F_{hk}|$ is an unknown phase α_{hk}; when that is known the structure is determined. Crystallographic analysis makes use of the atomic nature of matter to put constraints on α_{hk} such that the $|F_{hk}|$'s are self-consistent. Finding the positions of the atoms is the same as solving this "phase problem".

Crystal structure analysis must be broken into at least two stages: the final stage is always least-squares refinement to determine the best set of atomic positions (with error bars) that agrees with the observations. Unfortunately, this cannot be applied directly without some partial information about the structure, because of "false minima" in the least-squares functional. Getting close enough to the final solution for refinement to take over is where most of the effort is expended, and where most of the crystallographic techniques apply. In three-dimensional crystallography, the exact composition of the unit cell is normally known, but in surface work not even that is generally available, because an unknown number of layers is involved, and because stoichiometric changes are commonly involved with reconstruction (Bohr et al. 1985, Robinson 1983).

6.2. *Patterson function*

A good way to start analyzing the F_{hk}'s is to calculate the two-dimensional Patterson (pair correlation) function (Lipson and Cochran 1966, Patterson 1934),

$$P(x, y) = \sum_{hk} |F_{hk}|^2 \cos[2\pi(hx + ky)] \tag{34a}$$

$$\propto \int_0^{a_1} \int_0^{a_2} \rho_0(r_1, r_2)\, \rho_0(r_1 + a_1 x, r_2 + a_2 y)\, \mathrm{d}r_1\, \mathrm{d}r_2, \tag{34b}$$

where x and y are fractional coordinates along $\hat{r}_1$ and $\hat{r}_2$ which span the unit cell. Equation (34b) is true when all Fourier components are present, but the features of $P(x, y)$ becomes broadened when a truncated Fourier series is used. Patterson peaks separated by distances smaller than this resolution limit cannot be distinguished. $P(x, y)$ is usually represented as a contour map drawn on the real-space unit cell. It has the symmetry of the surface structure, provided all equivalents of the F_{hk}'s have been included, plus an additional centre of symmetry. It is usual to consider only the asymmetric repeating unit, which is some fraction of the full unit cell, as this contains all the information.

A positive peak in $P(x, y)$ at x_0, y_0 means that two or more atoms in the structure are separated by the vector (x_0, y_0). In simple cases, such as the example in fig. 17, an arrangement of atoms consistent with the Patterson may be determined by inspection. In general, however, an n-atom structure has $\frac{1}{2}n(n-1)$ independent vectors in the Patterson, and it may not be possible to interpret these in practice. Iterative procedures may then be used to find atoms one at a time, or else to search for known

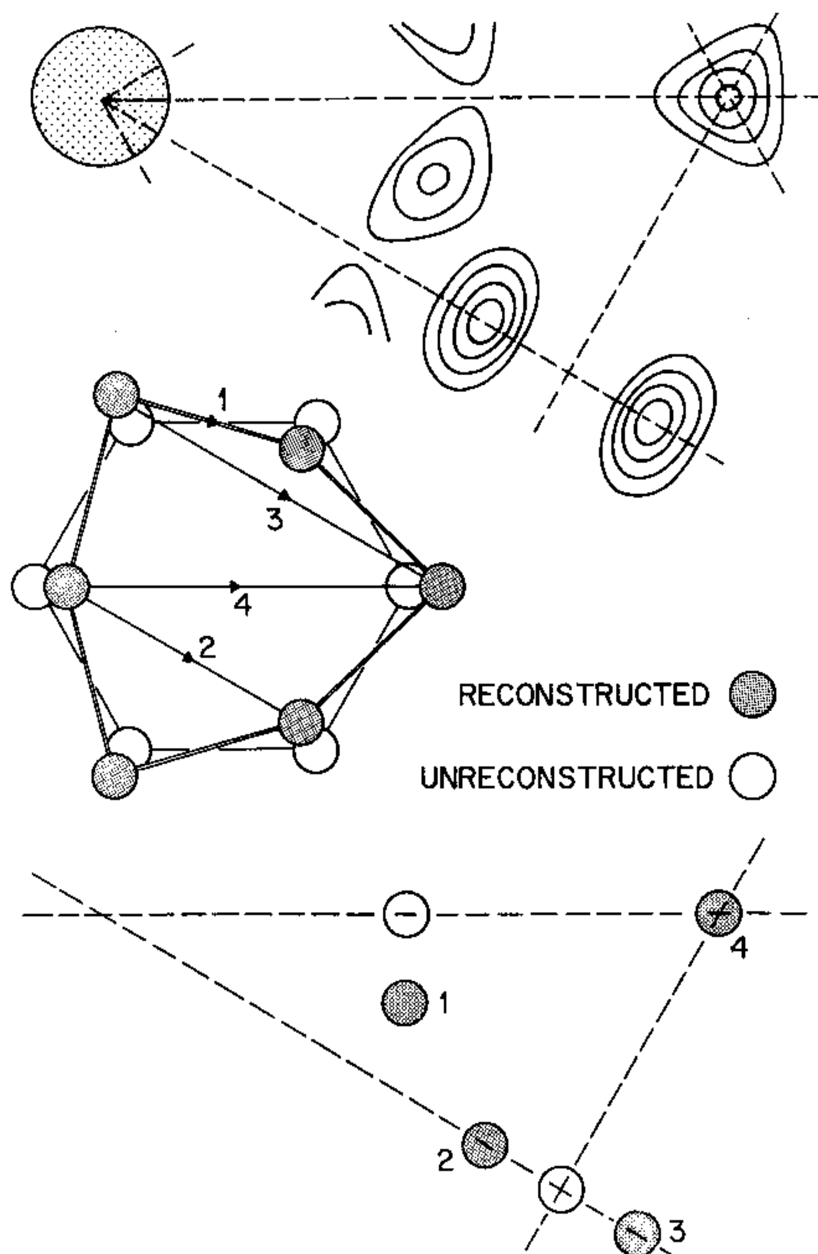

Fig. 17. Patterson function calculated from fractional order reflections measured on InSb(111)2 × 2 (Bohr et al. 1985). (a) Map showing equally spaced positive contours. The origin peak (shaded) rises 17 contour levels. The dashed lines are mirrors surrounding the asymmetric unit. (b) Interpretation of the map in terms of a distorted hexagon of atoms (shaded), derived from a (111) projection of the bulk structure (unshaded). (c) Interatomic vectors corresponding to (b), in good agreement with the observed peaks in (a).

components of a structure (e.g., molecules) systematically. Further details can be obtained in chapter 7 of Lipson and Cochran (1966).

A special problem that arises in surface-structure determination is one of missing integer-order data. This arises because these reflections fall on top of bulk reflections, either bulk Bragg peaks or crystal truncation rods (sect. 2.5). Unfortunately, these Fourier components of the surface structure are often strong and their omission can badly distort the Patterson. Negative peaks appear in the map which can cancel existing peaks, particularly near to the positions of bulk interatomic vectors. False peaks are not caused to appear, so a partial interpretation can still be made (Bohr et al. 1985, Robinson 1983, Bohr et al. 1986). While no structure should be based on evidence from a fractional-order Patterson alone, the method should be used to generate possible structures which can then be rigorously tested by structure-factor calculations. When accurate estimates of the unique-layer part of integer-order measurements can be separated from the crystal-truncation part (see sects. 2.6 and 6.5), more reliable Patterson functions will be attainable.

6.3. Agreement criteria

The ultimate test of any structure is its ability to reproduce the original observations. We use the definition of the structure factor [from eq. (3)],

$$F_{hk}^{\text{calc}} = \sum_{j=1}^{N_c} f_j \, \mathrm{e}^{2\pi i(hx_j + ky_j)}, \tag{35}$$

where the N_c atoms are at fractional coordinates (x_j, y_j). F_{hk}^{calc} has amplitude $|F_{hk}^{\text{calc}}|$ and phase $\alpha_{hk}^{\text{calc}}$. We test the agreement with observed structure factors, F_{hk}^{obs}, after adjusting a scale factor, by either the R-factor,

$$R = \frac{\sum |F_{hk}^{\text{obs}} - |F_{hk}^{\text{calc}}||}{\sum F_{hk}^{\text{obs}}}, \tag{36}$$

or a least-squares residual weighted according to the experimental uncertainty, σ_{hk},

$$\chi^2 = \frac{1}{N_{\text{obs}} - P} \sum_{hk} \frac{(F_{hk}^{\text{obs}} - |F_{hk}^{\text{calc}}|)^2}{\sigma_{hk}^2}. \tag{37}$$

N_{obs} is the number of observations in the sum and P is the number of parameters in the fit. R has the advantage of being absolute, allowing comparison from one structure to another; as mentioned above, it is very sensitive to which data are included and may be "tampered" by injudicious data screening. χ^2 is more meaningful from the error analysis point of view. It has a value of unity when the discrepancies are explained by experimental errors alone; a value greater than unity implies that a model is inadequate. It can never determine whether a model is "right", because the data may not be sufficiently good; it can, however, effectively rule out "wrong" models.

6.4. Difference map methods

The second method of crystallographic analysis that has been successfully applied to surface problems in the "difference synthesis" method (Cochran 1951). This is a

powerful method of using known pieces of a structure to find the remainder of the atoms. It is a convenient sequel to the Patterson method, when only part of a structure has been revealed. The basic assumption is that if the known part of a structure is close enough to the true structure, then the crystallographic phases generated by it are close to the true phases. A Fourier synthesis that uses observed amplitudes, $F_{hk}^{\rm obs}$, and calculated phases, $\alpha_{hk}^{\rm calc}$, then contains new information about the structure. Furthermore, a synthesis using *difference* coefficients,

$$D(x, y) = \sum_{hk} (F_{hk}^{\rm obs} - |F_{hk}^{\rm calc}|)\, e^{i\alpha_{hk}^{\rm calc}}\, e^{2\pi i(hx+ky)}, \tag{38}$$

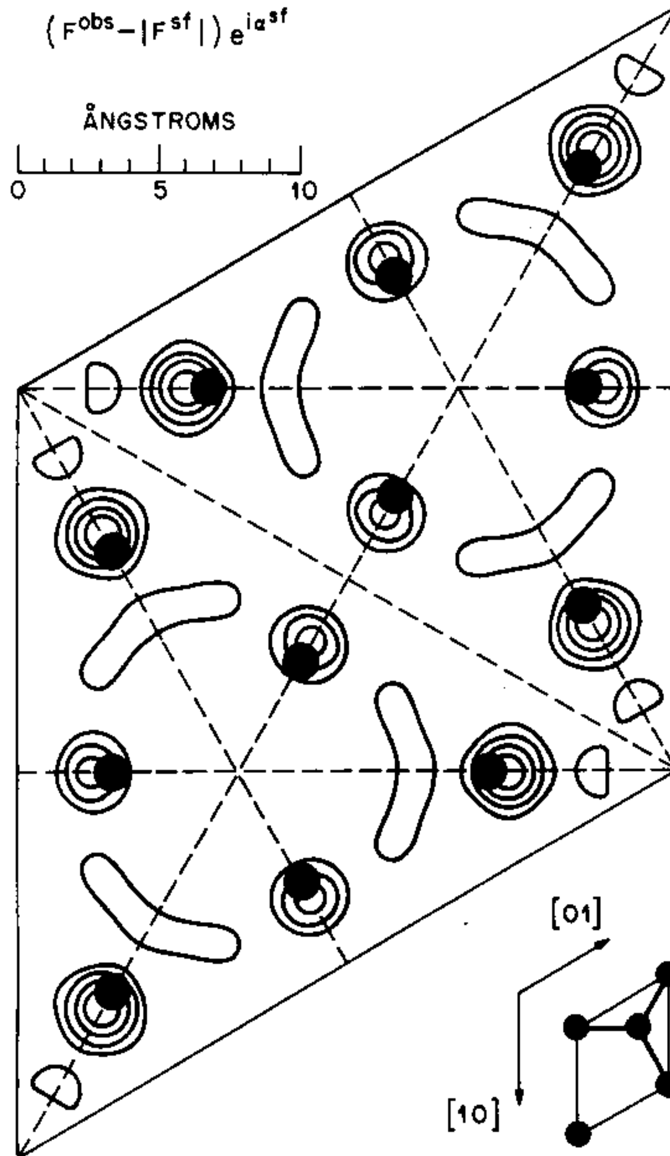

Fig. 18. Difference Fourier map for the Si(111)7 × 7 structure (Robinson et al. 1986a). Calculated amplitudes $|F^{\rm sf}|$ and phases $\alpha^{\rm sf}$ were obtained from a partial structure containing a stacking fault under half the unit cell. Positive contours (omitting the lowest) are shown over the entire 7 × 7 unit cell; a unit cell of the bulk (diamond) structure is shown bottom right. Twelve peaks are apparent, which indicate the need for extra atoms ("adatoms", shaded).

highlights in real space the differences between the true structure and the one input through the calculated amplitudes, $|F_{hk}^{calc}|$. Positive peaks in $D(x, y)$ indicate where extra atoms must be added while negative peaks signify deletions. Equations (35) and (38) need to be used iteratively since the modifications to the structure eventually result in changes in α_{hk}^{calc}. When the correct structure is used as a model, $D(x, y)$, has no peaks; the background fluctuation should be much lower than the atomic peaks of either a F_{hk}^{obs} or a F_{hk}^{calc} synthesis. An example of a difference Fourier map used to find positions of atoms in the Si(111)7 × 7 surface (Robinson et al. 1986a) is shown in fig. 18.

6.5. Experimental phase determination

Next we consider methods of determining the crystallographic phases experimentally.

6.5.1. Using the integer-order reflections

The first technique only concerns the integer-order reflections, which overlap with the crystal truncation rods (CTRs) and interfere with them. The structures factors of the CTRs can be calculated exactly, in amplitude and phase, from the bulk crystal structure. When these are compared with the observed values after adjusting a scale factor, there will, in general, be discrepancies due to the Fourier components F_{hk} of the unique surface layer. When the observed value is larger than expected, the two amplitudes are in phase, so $|F_{hk}|$ is taken to be the difference and α_{hk} to be the same as the CTR phase, α_{CTR}; when the observed value is smaller, they are out of phase, so α_{hk} is $\alpha_{CTR} + \pi$. A refinement of the method would involve fitting the integer-order rod profiles to extract the constant term from the $[\sin(\frac{1}{2}q_3 a_3)]^{-2}$ component. This method would be exact for centrosymmetric structures, in which the phases are 0 or π, but might be a good approximation in more general cases.

Although this method has not been used for *ab initio* phase determination, it has been used to determine the registry of a known surface structure, GaSb(111)2 × 2, with respect to its substrate (Feidenhans'l et al. 1986b). Six possible registries are allowed by its p3m1 symmetry. The intensities of integer-order reflections were compared with the superposition of a surface Fourier component and a bulk CTR, both known in amplitude but not in relative phase. Only one registry gave a satisfactory value of χ^2.

It was of some concern at the time that the widths of fractional order peaks were several times larger than the integer orders for this surface (Feidenhans'l et al. 1986b), and that the CTR analysis worked in spite of this. The widths of the fractional orders are determined by a distribution of antiphase domains of 2 × 2 structure on the surface, but these domains are in phase with each other at integer-order positions. Provided the peaks are integrated correctly, this does not distort the analysis. It has also been shown that the superposition of amplitudes for the reconstructed layer and the CTR is still valid for rough surfaces where the coherence is limited by the presence of steps (Vlieg et al. 1989a).

6.5.2. Heavy-atom method

Another method of phase determination, which is well-suited to surface problems, involves systematically modifying the contents of the unit cell with heavy atoms.

Ideally, a single heavy atom should be added to each cell (Lipson and Cochran 1966). In practice, this can be achieved by physisorption of an inert gas, controlling the temperature and vapour pressure to adjust the coverage. Chemisorption may also be used, at a risk of disturbing the surface structure under examination. If adsorbate systems are the object of study, the dependence of the observed structure factors upon coverage can yield the same information. Heavy atoms can assist structure determination in several ways, in addition to simply increasing the signal rate. If there is a single binding site per unit cell, the Patterson becomes straightforward to interpret, because all the strong peaks involve the heavy atom; the Patterson is then just an image of the contents of the unit cell. An equivalent statement is that the phases of all the structure factors are zero if the atom is sufficiently heavy. Multiply substituted arrangements of heavy atoms can be solved from the Patterson, then used to phase the whole structure, again by assuming that they dominate the scattering. A more sophisticated variation is to measure structure factors both with and without the heavy atom, then use the sign of the difference to determine the phase (Blow and Rossmann 1961). For centrosymmetric structures this method is exact, and otherwise leads to a sign ambiguity which can be resolved by use of a second heavy atom derivative (Blundell and Johnson 1976). The heavy-atom method is formally analogous to the optical imaging technique of holography.

The heavy atom method has been used to solve the structure of the Si(111)-Bi$\sqrt{3} \times \sqrt{3}$ surface (Takahashi et al. 1987a,b). The Bi is so much heavier than the Si that it dominates the phase of all reflections and allows the positions of the latter to be determined directly. The experiments use a novel geometry for surface X-ray diffraction, energy dispersive back-reflection at fixed scattering angle (Takahashi et al. 1987a,b). Synchrotron radiation is essential for this technique.

6.5.3. Anomalous scattering

Another technique, which applies to structures containing more than one kind of atom, is the use of anomalous dispersion, or the wavelength dependence of the atomic form factor. The differences between structure factors measured at two wavelengths, one below and one just above the absorption edge of the element concerned, are analyzed for the positions of those atoms alone. The positions of all the other atoms are then determined in a way analogous to the heavy-atom method. One variant of the technique is to use F_{hk}, $F_{\bar{h}\bar{k}}$ pairs (Friedel pairs) which differ because of the imaginary component of the form factor near the absorption edge (Stout and Jensen 1968, Blundell and Johnson 1976). Another variant is to use three wavelengths; a direct measure of the phase can then be derived (Chapuis et al. 1985). The methods work best when a small number of anomalously scattering atoms are present in the unit cell; for this reason and because of bulk fluorescent background problems, it is probably best to use an adsorbed atom, unique to the surface, as the anomalous scatterer.

6.6. Direct methods

Finally, we should mention crystallographic "direct methods". Their use in surface crystallography is largely unexplored, but they are the routine choice in small-

molecule crystallography. The prerequisite for success is that the data be accurate (preferably 2%) and numerous (preferably a ten fold redundancy over the number of atoms in the asymmetric unit). Direct methods are based on probabilistic relationships between structure factors which derive ultimately from the fact that crystalline matter has an electron density which is real, positive and clustered into atoms. Sayre (1952) showed that the structure factors of a crystal containing equally sized, point-like atoms are interrelated by

$$F_{hk} = \phi \sum_{h'k'} F_{h'k'} F_{h-h',k-k'}, \tag{39}$$

where ϕ is a slow-varying function related to atomic form factors. Equation (39) is dominated by the largest terms so, for a centrosymmetric structure, the signs (phases) of large Fs are correlated as

$$\mathrm{Sign}(F_{hk}) \approx \mathrm{Sign}(F_{h'k'})\,\mathrm{Sign}(F_{h-h',k-k'}), \tag{40}$$

where the "$\approx$" symbol means "probably equals". The probability of truth of eq. (40) is expressed as a monotonic function of the product of the magnitude of the three structure factors involved (Cochran and Woolfson 1955), and is very close to unity for the largest "triplets" in general. Practical methods for bootstrap phasing of entire sets of data have become well developed (Stout and Jensen 1968, Lipson and Cochran 1966).

Karle and Hauptman (1956) have derived analogous equations (called "tangent formulae") relating the phases of triplets of strong structure factors in non-centrosymmetric structures. Fully automatic routines for the application to *ab initio* phasing have been developed and are in widespread use (Karle and Karle 1966). It has recently been shown by Bricogne (1984) that the tangent formula is just the first-approximation solution to a general formalism wherein the set of true phases occupies a maximum of an "entropy" functional. An entirely new procedure for crystallographic phasing by the maximum entropy method is being developed (Bricogne 1984).

6.7. *Refinement*

Once the "phase problem" has been solved for a given case and an atomic model of the structure has been obtained, the final step required is least-squares refinement of all the free parameters in the model. Computational methods for non-linear least squares refinement are widely available (Bevington 1969). The least-squares residual, χ^2, which optimally includes all of the crystallographic information is given above in eq. (37); this reaches the minimum value of unity only when a sufficiently general model is used. The number of meaningful parameters that may be extracted from the model before χ^2 falls to unity depends upon the number of data and their accuracy. When a parameter is added to a model, the agreement between F_{obs} and F_{calc} always improves. However, since P is increased by 1 in eq. (37), the value of χ^2 does not necessarily drop; when it does not, the extra parameter is not statistically significant. In some cases, it may not be possible even to uniquely determine all of the atomic coordinates, and some simplifying assumptions, such as knowledge of the coordination chemistry, must be made in the model (Robinson et al. 1986a). In other cases,

χ^2 may still not have fallen to unity when all of the atomic positions are fixed; it is then important to consider the effects of thermal motion and partial occupancy.

6.7.1. Thermal motion

Proper accounting for thermal motions has not been mentioned before, even although it is needed almost always in crystallographic analysis. The effect on the structure factor is a straightforward multiplication of each atomic form factor by a Debye–Waller factor (Debye 1914, Warren 1969),

$$e^{-M} = e^{-B\sin^2\theta/\lambda^2} = e^{-\frac{1}{2}q^2\langle u_x^2\rangle} \tag{41}$$

where $B = 8\pi^2\langle u_x^2\rangle$ is called the temperature factor and $\langle u_x^2\rangle$ is the mean square component of vibration of the atom along the direction of the momentum transfer. Depending on the accuracy of the data, it may be possible to extract a single B for all the atoms of the structure, individual Bs for each atom, or even six components of a B tensor describing anisotropic thermal motion. In practice, with the earliest surface problems studied, a value of $\langle u_x^2\rangle^{1/2}$ of 0.13 ± 0.03 Å was obtained for the atoms of the reconstructed Au(110) surface at room temperature (Robinson 1983), compared with 0.084 Å for bulk Au. This is clearly a demonstration of surface-enhanced thermal vibration. In contrast, the value of 0.12 Å obtained for InSb(111)2 × 2 (Bohr et al. 1985) is within error of the bulk value of 0.13 Å.

6.7.2. Partial occupancy

Partial occupancy is likely to be a common feature of surface structures, because of the uncertainties of surface preparation techniques. In a structure factor calculation, it may be, therefore, necessary to include multiplicative occupancy parameters $0 < \beta_j < 1$ for each atom j in the unit cell. Variable occupancy arguments were used in the analysis of Si(111)7 × 7 (Robinson et al. 1986a) to prove that one adatom per site was needed. A more dramatic example was the determination of fractional substitution of Ge by Sn for every site of the Ge(111)–Sn7 × 7 structure (Skov Pedersen et al. 1988, Skov Pedersen 1988). Since surface stoichiometry is generally unknown in a given problem, variable occupancies should be included in structural models in order to get unambiguous results.

6.7.3. Error bars

Parameter error bars can be obtained directly from the correlation matrix in the least-squares calculation (Bevington 1969) or else in a more intuitive way by plotting the variation of χ^2 with each parameter: a conservative error bar can then be taken as the range of parameter values over which χ^2 is less than *double* its minimum value (Bohr et al. 1985). With larger structures, the effect of moving (or even removing) one atom will be less, and it may be necessary to use $\chi^2 < 1.5\chi^2_{\min}$ as the criterion (Robinson et al. 1986a).

6.7.4. Real-space refinement

The computer time needed to refine large structures by traditional non-linear least-squares methods (Bevington 1969) is not insignificant. Most of the time is spent

calculating trigonometric functions in evaluating the $F_{hk}^{\rm calc}$'s and their derivatives. Because this problem arises frequently in crystallography, considerable efforts have been made to find ways to optimize the calculation. Notable savings have been made by block-diagonalization (Hodgson and Rollett 1963) or by using fast Fourier transforms (Agarwal 1978). Cochran (1948) showed that least-squares refinement in reciprocal space is formally identical to fitting atomic models into density obtained by Fourier transformation, although this no longer allows use of the experimental weighting. More recently, methods have been developed that simultaneously minimize chemical constrains (in the form of an "energy") and crystallographic data in techniques of "real-space refinement" (Diamond 1971, Jack and Levitt 1978, Konnert 1976). All of these may become useful in surface problems in the near future.

6.8. Special crystal truncation rod techniques

We include this discussion as a separate section, because of some basic differences that should be emphasized. We have already seen at the beginning of this section how *fractional*-order rods can be incorporated in a structure analysis, and also in sect. 6.5.1 how CTRs can be used to test registry of a surface with respect to the bulk. Because of the special q_3 dependence of the CTRs in eq. (14), it is not possible to include them in a conventional crystallographic analysis. Two ways of avoiding this problem have been developed.

6.8.1. Rod profile analysis

The object here is to calculate the CTR amplitude for a general (bulk) crystal structure in the form of a CTR structure factor which can be added to the structure of the surface layer (as a complex quantity). The most convenient way to achieve this is to redefine the bulk unit cell with its $\hat{r}_3$-axis perpendicular to the surface. Cubic Si for a Si(111) surface, therefore, becomes hexagonal with six atoms (three double layers) in the unit cell; Si(100) becomes tetragonal with four atoms each in a different layer. We can write the CTR amplitude as a sum over layers in the perpendicular direction, which factorizes into a sum over unit cells and a sum over the N_c atoms inside the new unit cell.

$$F_{hk}^{\rm CTR}(l) = \sum_{j'=1}^{\infty} e^{iq_3 a_3 j'} \sum_{j=1}^{N_c} f_j(q)\, e^{i\boldsymbol{q}\cdot\boldsymbol{r}_j} = \frac{1}{1 - e^{iq_3 a_3 j'}}\, F_{\rm cell}(\boldsymbol{q}). \tag{42}$$

Systematic absences will be correctly handled by this representation: the numerator and denominator of eq. (42) both go to zero simultaneously, leaving a smooth function. One curious note is that, because $F_{hk}^{\rm CTR}(l)$ is now a continuous function of l, it is important that the origin of the unit cell be the top layer. The CTR for Si(111) ending with a double layer is totally different from that ending with a single layer.

Adding the structure factor for the surface layer or layers to eq. (42) gives the complete description of the CTR intensity. Fit parameters, such as layer spacings and fractional occupations, can be extracted by least-squares refinement against the observed profiles. Analysis even of unreconstructed ('1 × 1') surfaces and interfaces is possible.

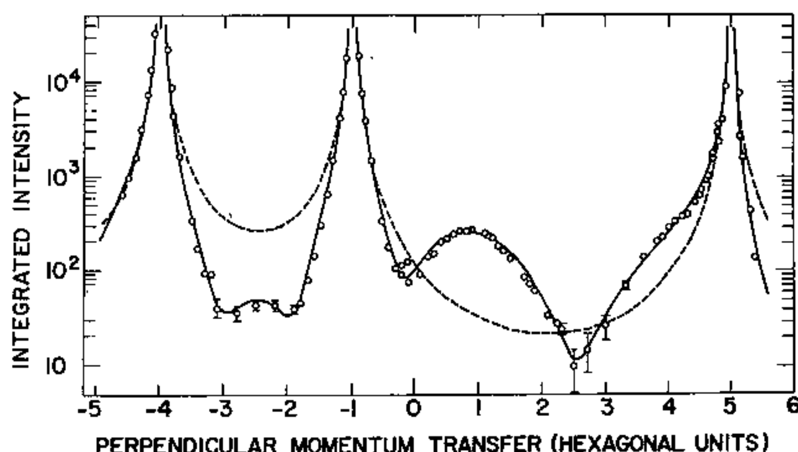

Fig. 19. The $(1, 0, l)$ crystal truncation rod (hexagonal indexing scheme) for a Si(111)7 × 7–a-Si interface as a function of perpendicular momentum transfer, l. Three Bragg peaks at (220), $(11\bar{1})$ and $(\bar{1}\bar{1}\bar{3})$ in cubic units are crossed, along with a systematic absence at $(00\bar{2})$. The curve is a fit to the data from a four-layer model of the interface (Robinson et al. 1986b).

Several examples of this kind have been studied. Accurate layer spacings and occupancies were obtained for the Si(111)–a-Si interface (Robinson et al. 1986b). Figure 19 shows the agreement between experiment and calculation. Measurements of the $(0, 0, l)$ truncation rod for Au(001) show marked asymmetry about the (002) Bragg peak; this result is explained in terms of a top layer of greater density shifted outwards by about 20% of a layer spacing (Gibbs et al. 1988). The $(0, 0, l)$ truncation rod crosses over to a reflectivity measurement at small l, and this region is also explained well by the theory when appropriate normalization is used. Figure 20 shows

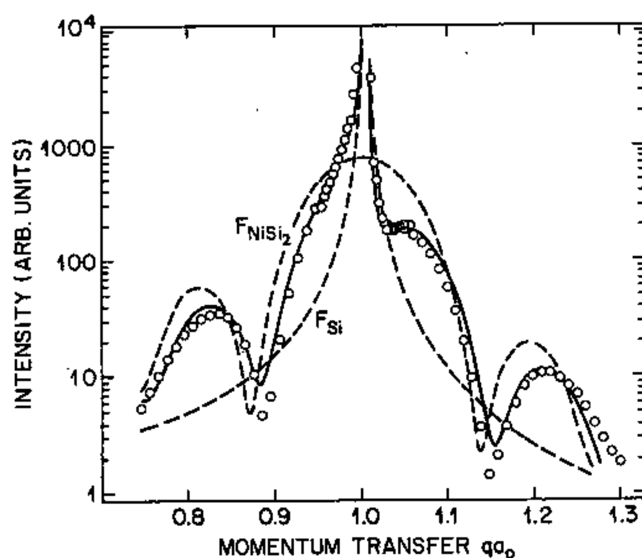

Fig. 20. Specular truncation rod through the (111) Bragg peak of a seven-layer $NiSi_2$(111) film grown on Si(111). The interfacial separation gives rise to a profound asymmetry in the region where the CTR and overlayer peak have the same intensity (Robinson et al. 1988). Dashed curves indicate the individual contributions of the substrate and film.

the specular truncation rod of the interface of a 7-layer $NiSi_2(111)$ film on a Si(111) substrate. The interference of the substrate CTR and the broad rod-like (111) Bragg peak of the film results in a highly asymmetric lineshape that depends sensitively on the interfacial separation (Robinson et al. 1988).

6.8.2. *In-plane analysis with CTRs*

Here we will derive the value of the *in-plane* CTR amplitude in such a way that it can be included in a standard structure factor calculation: the coordinates of a set of "fake" atoms that generates (in amplitude and phase) the CTRs correctly. This is most useful when conventional three-dimensional crystallographic software is used without alteration. The method only works at $l=0$ (in-plane condition) and for reflections that are not allowed in the bulk. It, therefore, does not apply to primitive crystal classes (e.g., simple cubic). We calculate the next two most common cases: fcc or bcc(001) and fcc(111).

(a) Centred cubic (001) face

Here we choose, without loss of generality, a tetragonal unit cell with two atoms at (000) and $(\frac{1}{2}\frac{1}{2}\frac{1}{2})$. Substituting in eq. (42), using crystallographic nomenclature for $q=(2\pi h/a_1, 2\pi k/a_2, 2\pi l/a_3)$,

$$F_{hk}^{\mathrm{CTR}}(l)=\frac{f}{1-\mathrm{e}^{2\pi i l}}\left[1+\mathrm{e}^{2\pi i(\frac{1}{2}h+\frac{1}{2}k+\frac{1}{2}l)}\right]. \tag{43}$$

When $h+k$ is even, we have a bulk Bragg peak at $l=0$, so we consider only $h+k$ odd;

$$F_{hk}^{\mathrm{CTR}}(0)=\lim_{l\to 0} F_{hk}^{\mathrm{CTR}}(l)=\tfrac{1}{2}f. \tag{44}$$

Hence we can replace the entire semi-infinite crystal by a single atom at the position of its top layer with an effective form factor of one half the normal value. We are then free to add in extra layers of atoms containing, e.g., a reconstruction, and know that the CTRs will be calculated correctly at $l=0$.

(b) Face-centered cubic (111)

Using a hexagonal unit cell, we have three atoms at (000), $(\frac{1}{3}\frac{2}{3}\frac{1}{3})$ and $(\frac{2}{3}\frac{1}{3}\frac{2}{3})$,

$$F_{hk}^{\mathrm{CTR}}(l)=\frac{f}{1-\mathrm{e}^{2\pi i l}}\left(1+\mathrm{e}^{2\pi i(\frac{1}{3}h+\frac{2}{3}k+\frac{1}{3}l)}+\mathrm{e}^{2\pi i(\frac{2}{3}h+\frac{1}{3}k+\frac{2}{3}l)}\right). \tag{45}$$

The in-plane Bragg peaks occur when $2h+k=3n$ for integer n. The remaining cases give us the in-plane CTRs;

$$F_{hk}^{\mathrm{CTR}}(0)=\lim_{l\to 0} F_{hk}^{\mathrm{CTR}}(l)=\tfrac{2}{3}f+\tfrac{1}{3}f\,\mathrm{e}^{2\pi i(\frac{1}{3}h+\frac{2}{3}k)}. \tag{46}$$

This is most easily seen by expanding the exponentials in l and taking the limit $l\to 0$. Thus, the semi-infinite bulk crystal is replaced by its top layer with an effective form factor $\frac{2}{3}f$ plus its second layer with $\frac{1}{3}f$.

7. Conclusions

We have discussed in considerable detail the principles of X-ray diffraction from surfaces and the experimental methods used to make crystallographic determinations of surface structures. Space does not permit a comparison of X-ray diffraction with other techniques sensitive to surface structure, except to emphasize that it is a long-range probe. This has advantages and disadvantages: the Fourier transform property of diffraction acts as a powerful filter, selecting the crystalline ordered regions of the surface while disregarding defects and (to a large extent) contamination. At the same time, it will be very difficult to obtain information about localized features of surfaces, such as steps or isolated dislocations, that, e.g., the scanning tunnelling microscope sees very clearly. Some progress has, however, been made in studying line defects on surfaces using analysis of X-ray diffraction lineshapes (Robinson and D'Amico 1985). There has also been a growing body of literature on surface phase transitions using X-ray diffraction lineshapes. This has not been discussed in this chapter, except to the extent that the experimental hardware is very similar (Horn et al. 1978, McTague et al. 1982, Held et al. 1987, Mochrie 1987, Chung et al. 1987).

The list of published work in surface crystallography is fairly short, but expected to grow rapidly. Surfaces that have been studied are (in approximate chronological order) Ge(100)2 × 1 (Eisenberger and Marra 1981, Grey et al. 1988), Pb overlayers on Cu(110) (Marra et al. 1982, Brennan et al. 1986). Au(110)1 × 2 (Robinson 1983, Robinson et al. 1984), InSb(111)3 × 3 (Johnson et al. 1985), O–Cu(110)2 × 1 (Liang et al. 1985), InSb(111)2 × 2 (Feidenhans'l et al. 1985, Bohr et al. 1985), Si(111)7 × 7 (Robinson 1985, Robinson et al. 1986a), W(100) (Robinson 1986, Altman et al. 1988), Pb–Ge(111) (Feidenhans'l et al. 1986a), GaSb(111)2 × 2 (Feidenhans'l et al. 1986b), Sn–Ge(111) (Skov Pedersen et al. 1988, Skov Pedersen 1988), Ge(111)c2 × 8 (Feidenhans'l et al. 1988), Bi–Si(111)$\sqrt{3} \times \sqrt{3}$ (Takahashi et al. 1987a,b), Au(001) (Gibbs et al. 1988), Pb–Cu(001) (Liang et al. 1988b), Ag–Si(111)$\sqrt{3} \times \sqrt{3}$ (Vlieg et al. 1988b), Sn–Si(111)$\sqrt{3} \times \sqrt{3}$ (Conway et al. 1989), TiO_2(100)1 × 3 (Zschack et al. 1989) and GaAs(001)c4 × 4 (Sauvage-Simkin et al. 1989). Some of these have been used as examples here, but the main structural results (Fuoss et al. 1986, Feidenhans'l 1989) as well as general descriptions of the technique (Nielsen 1985, Grey and Feidenhans'l 1988) are reviewed elsewhere.

References

Afanas'ev, A.M., and M.K. Melkonyan, 1983, Acta Crystallogr. A **39**, 207.
Agarwal, R.C., 1978, Acta Crystallogr. A **34**, 791.
Akimoto, K., J. Mizuki, T. Tatsumi. N. Aizaki and J. Matsui, 1987, Surf. Sci. **183**, L297.
Akimoto, K., J. Mizuki, I. Hirosawa and J. Matsui, 1989, Rev. Sci. Instrum. **60**, 2362.
Altman, M.S., P.J. Estrup and I.K. Robinson, 1988, Phys. Rev. B **38**, 5211.
Becker, R.S., J.A. Golovchenko and J.R. Patel, 1983, Phys. Rev. Lett. **50**, 153.
Bevington, P.R., 1969, Data Reduction and Error Analysis for the Physical Sciences (McGraw-Hill, New York).
Bloch, J.M., 1985, J. Appl. Crystallogr. **18**, 33.

Blow, D.M., and M.G. Rossmann, 1961, Acta Crystallogr. **14**, 1195.
Blundell, T.L., and L.N. Johnson, 1976, Protein Crystallography (Academic Press, New York).
Bohr, J., R. Feidenhans'l, M. Nielsen, M. Toney, R.L. Johnson and I.K. Robinson, 1985, Phys. Rev. Lett. **54**, 1275.
Bohr, J., R. Feidenhans'l, M. Nielsen, M. Toney, R.L. Johnson and I.K. Robinson, 1986, Phys. Rev. Lett. **56**, 2878.
Born, M., and E. Wolf, 1975, Principles of Optics (Pergamon Press) pp. 36–41.
Braslau, A., 1987, SPEC program, PhD dissertation Harvard University, available from G. Swislow (Certified Scientific Software, Cambridge, MA).
Brennan, S., and P. Eisenberger, 1984, Nucl. Instrum. & Methods **222**, 164.
Brennan, S., P.H. Fuoss and P. Eisenberger, 1986, Phys. Rev. B **33**, 3678.
Bricogne, G., 1984, Acta Crystallogr. **40**, 410.
Budai, J., P.D. Bristowe and S.L. Sass, 1983, Acta Metall. **31**, 644.
Buerger, M.J., 1960, Crystal Structure Analysis (Wiley, New York).
Busing, W.R., and H.A. Levy, 1967, Acta Crystallogr. **22**, 457.
Chapuis, G., D.H. Templeton and L.K. Templeton, 1985, Acta Crystallogr. A **41**, 274.
Chung, J.W., K. Evans-Lutterodt, E.D. Specht, R.J. Birgeneau, P.J. Estrup and A.R. Kortan, 1987, Phys. Rev. Lett. **59**, 2192.
Claverie, P., 1986, Ph.D. dissertation (Université de Clermont).
Cochran, W., 1948, Acta Crystallogr. **1**, 138.
Cochran, W., 1951, Acta Crystallogr. **4**, 408.
Cochran, W., and M.M. Woolfson, 1955, Acta Crystallogr. **8**, 1.
Conway, K.M., J.E. Macdonald, C. Norris, E. Vlieg and J.F. van der Veen, 1989, Surf. Sci. **215**, 555.
Cowan, P.L., 1985, Phys. Rev. B **32**, 5437.
D'Amico, K.L., D.E. Moncton, E.D. Specht, R.J. Birgeneau, S.E. Nagler and P.M. Horn, 1984, Phys. Rev. Lett. **53**, 2250.
Debye, P.W.J., 1914, Ann. Phys. **43**, 49.
Diamond, R., 1971, Acta Crystallogr. A **27**, 436.
Dietrich, S., and H. Wagner, 1984, Z. Phys. (Germany) B **56**, 207.
Dutta, P., J.B. Peng, B. Lin, J.B. Ketterson, M. Prakash, P. Georgopoulos and S. Ehrlich, 1987, Phys. Rev. Lett. **58**, 2228.
Eisenberger, P., and W.C. Marra, 1981, Phys. Rev. Lett. **46**, 1081.
Erbil, A., A.R. Kortan, R.J. Birgeneau and M.S. Dresselhaus, 1983, Phys. Rev. B **28**, 6329.
Feidenhans'l, R., 1986, Ph.D. Thesis (Riso&sl; National Laboratory).
Feidenhans'l, R., 1989, Surf. Sci. Rep. **10**, 105.
Feidenhans'l, R., J. Bohr, M. Nielsen, M. Toney, R.L. Johnson, F. Grey and I.K. Robinson, 1985, Festkoerperprobleme XXV, 545.
Feidenhans'l, R., M. Nielsen, F. Grey and R.L. Johnson, 1986a, Surf. Sci. **178**, 927.
Feidenhans'l, R., M. Nielsen, F. Grey, R.L. Johnson and I.K. Robinson, 1986b, Surf. Sci. **186**, 499.
Feidenhans'l, R., J.S. Pedersen, J. Bohr, M. Nielsen, F. Grey and R.L. Johnson, 1988, Phys. Rev. B **38**, 9715.
Fleming, R.M., 1985, Super Diffractometer Control Program, unpublished.
Fuoss, P.H., 1983, in: Synchrotron Radiation and Surface Science, eds. D. Norman and J.E. Inglesfield, Daresbury Report DL/SCI//R21.
Fuoss, P.H., and I.K. Robinson, 1984, Nucl. Instrum. & Methods **222**, 171.
Fuoss, P.H., K.S. Liang and P. Eisenberger, 1986, in: Synchrotron Radiation Research: Advances in Surface and Low Dimensional Science, ed. R.Z. Bachrach (Plenum Press, New York).
Gibbs, D., B.M. Ocko, D.M. Zehner and S.G.J. Mochrie, 1988, Phys. Rev. B **38**, 7303.
Gibbs, L.D., S. Ulc, A. Meade, J.D. Axe and D.E. Moncton, 1986, unpublished.
Gibson, J.M., H.J. Gossmann, J.C. Bean, R.T. Tung and L.C. Feldman, 1986, Phys. Rev. Lett. **56**, 355.
Golovin, A.L., and R.M. Imamov, 1984, Sov. Phys. Crystallogr. **29**, 249.
Grant, D.F., R.C.G. Killean and J.L. Lawrence, 1969, Acta Crystallogr. B **25**, 374.
Grey, F., and R. Feidenhans'l, 1988, Europhysics News **19**, 94.

Grey, F., R.L. Johnson, R. Feidenhans'l, J.S. Pedersen and M. Nielsen, 1988, in: Structure of Surface II, eds J.F. van der Veen and M.A. van Hove (Springer, Berlin) pp. 292–297.
Guinier, A., 1963, X-ray Diffraction (W.H. Freeman & Co., San Francisco, CA).
Held, G.A., J.L. Jordan-Sweet, P.M. Horn, A. Mak and R.J. Birgeneau, 1987, Phys. Rev. Lett. **59**, 2075.
Hodgson, L.I., and J.S. Rollett, 1963, Acta Crystallogr. **16**, 329.
Horn, P.M., R.J. Birgeneau, P. Heiney and E.M. Hammonds, 1978, Phys. Rev. Lett. **41**, 961.
Howell, J.A., and P. Horowitz, 1975, Nucl. Instrum. & Methods **125**, 225.
Imamov, R.M., A.L. Golovin, S.A. Stepanov and A.M. Afanas'ev, 1983, Proc. Int. Ion. Eng. Cong., ISIAT 1983, Kyoto.
Jack, A., and M. Levitt, 1978, Acta Crystallogr. A **34**, 931.
Jackson, J.D., 1975, Classical Electrodynamics (Wiley, New York).
Jagodzinski, H., 1949, Acta Crystallogr. **2**, 201.
James, R.W., 1955, The Optical Principles of the Diffraction of X-rays (Cornell University Press, Ithaca, NY).
Johnson, R.L., J.H. Fock, I.K. Robinson, J. Bohr, R. Feidenhans'l, J. Als-Nielsen, M. Nielsen and M. Toney, 1985, in: The Structure of Surfaces, eds M.A. van Hove and S.Y. Tong (Springer, Berlin) pp. 313–316.
Karle, J., and H. Hauptman, 1956, Acta Crystallogr. **9**, 635.
Karle, J., and I.L. Karle, 1966, Acta Crystallogr. **21**, 849.
Kikuta, S., and K. Kohra, 1970, J. Phys. Soc. Jpn. **29**, 1322.
Kishino, S., and K. Kohra, 1971, Jpn. J. Appl. Phys. **10**, 551.
Kjaer, K., J. Als-Nielsen, C.A. Helm, L.A. Laxhuber and H. Möhwald, 1987, Phys. Rev. Lett. **58**, 2224.
Konnert, J.H., 1976, Acta Crystallogr. A **32**, 614.
Krebshmar, F., and D. Wolf, 1986, unpublished.
Liang, K.S., P.H. Fuoss, G.J. Hughes and P. Eisenberger, 1985, in: The Structure of Surfaces, eds M.A. van Hove and S.Y. Tong (Springer, Berlin).
Liang, K.S., K.L. D'Amico and J. Russo, 1988a, unpublished.
Liang, K.S., E.B. Sirota, G.J. Hughes, K.L. D'Amico and P. Eisenberger, 1988b, in: Structure of Surfaces II, eds J.F. van der Veen and M.A. van Hove (Springer, Berlin) pp. 509–513.
Lipson, H., and W. Cochran, 1966, The Determination of Crystal Structures (Cornell University Press, Ithaca, NY).
Marra, W.C., 1981, Ph.D. Thesis (Stevens Institute).
Marra, W.C., P. Eisenberger and A.Y. Cho, 1979, J. Appl. Phys. **50**, 6927.
Marra, W.C., P.H. Fuoss and P. Eisenberger, 1982, Phys. Rev. Lett. **49**, 1169.
McTague, J.P., J. Als-Nielsen, J. Bohr and M. Nielsen, 1982, Phys. Rev. B **25**, 7765.
Mochrie, S.G.J., 1987, Phys. Rev. Lett. **59**, 304.
Mochrie, S.G.J., 1988, J. Appl. Cryst. **21**, 1.
Moncton, D.E., and G.S. Brown, 1983, Nucl. Instrum. & Methods **208**, 579.
Moncton, D.E., and R. Pindak, 1979, Phys. Rev. Lett. **43**, 701.
Moncton, D.E., R. Pindak, S.C. Davey and G.S. Brown, 1982, Phys. Rev. Lett. **49**, 1865.
Nielsen, M., 1985, Z. Phys. **61**, 415.
Norris, C., J.S.G. Taylor, P.R. Moore and N.W. Harris, 1987, unpublished.
Patterson, A.L., 1934, Phys. Rev. **46**, 372.
Post, B., 1979, Acta Crystallogr. A **35**, 17.
Riley, K.F., 1974, Mathematical Methods for the Physical Sciences (Cambridge University Press, Cambridge).
Robinson, I.K., 1983, Phys. Rev. Lett. **50**, 1145.
Robinson, I.K., 1985, in: Structure of Surfaces, eds M.A. van Hove and S.Y. Tong (Springer, Berlin) pp. 60–65.
Robinson, I.K., 1986, Phys. Rev. B **33**, 3830.
Robinson, I.K., 1987, Phys. Rev. B **35**, 3910.
Robinson, I.K., 1988, Aust. J. Phys. **41**, 359.
Robinson, I.K., 1989, Rev. Sci. Instrum **60**, 1541.
Robinson, I.K., and K.L. D'Amico, 1985, in: Advanced Photon and Particle Techniques for the

Characterization of Defects in Solids, Vol. 41, ed. J.B. Roberto (Materials Research Society) pp. 161–170.
Robinson, I.K., Y. Kuk and L.C. Feldman, 1984, Phys. Rev. B **29**, 4762.
Robinson, I.K., W.K. Waskiewicz, P.H. Fuoss, J.B. Stark and P.A. Bennett, 1986a, Phys. Rev. B **33**.
Robinson, I.K., W.K. Waskiewicz, R.T. Tung and J. Bohr, 1986b, Phys. Rev. Lett. **57**, 2714.
Robinson, I.K., R.T. Tung and R. Feidenhans'l, 1988, Phys. Rev. B **38**, 3632.
Samant, M.G., M.F. Toney, G.L. Borges, L. Blum and O.R. Melroy, 1988, Surf. Sci. **193**, L29.
Sass, S.L., 1980, J. Appl. Crystallogr. **13**, 109.
Sauvage-Simkin, M., R. Pinchaux, J. Massies, P. Claverie, N. Jedrecy, J. Bonnet and I.K. Robinson, 1989, Phys. Rev. Lett. **62**, 563.
Sayre, D., 1952, Acta Crystallogr. **5**, 60.
Skov Pedersen, J., 1988, Ph.D. dissertation (University of Copenhagen).
Skov Pedersen, J., R. Feidenhans'l, M. Nielsen, F. Grey and R.L. Johnson, 1988, Phys. Rev. B **38**, 13210.
Stephens, P.W., and P. Eng, 1988, unpublished.
Stout, G.H., and L.H. Jensen, 1968, X-ray Structure Determination (Macmillan, New York).
Takahashi, T., S. Nakatani, T. Ishikawa and S. Kikuta, 1987a, Surf. Sci. **191**, L825.
Takahashi, T., S. Nakatani, T. Ishikawa and S. Kikuta, 1987b, Surf. Sci. **183**, L302.
van Hove, M.A., and S.Y. Tong, 1979, Surface Crystallography by LEED (Springer, Berlin).
Vineyard, G., 1982, Phys. Rev. B **26**, 4146.
Vlieg, E., J.F. van der Veen, J.E. Macdonald and M. Miller, 1987a, J. Appl. Cryst. **20**, 330.
Vlieg, E., A. van 't Ent, A.P. de Jongh, H. Neerings and J.F. van der Ven, 1987b, Nucl. Instrum. & Methods A **262**, 522.
Vlieg, E., J.F. van der Veen, S.J. Gurman, C. Norris and J.E. Macdonald, 1989a, Surf. Sci. **210**, 301.
Vlieg, E., A.W. Denier van der Gon, J.F. van der Veen, J.E. Macdonald and C. Norris, 1989b, Surf. Sci. **209**, 100.
Warren, B.E., 1969, X-ray Diffraction (Addison-Wesley, Reading, MA).
Zschack, P., J.B. Cohen and Y.W. Chung, 1989, J. Appl. Cryst. **21**, 466.